Axial and torsional self-excited vibrations of a distributed drill-string

Journal of Sound and Vibration 444 (2019) 127–151

Contents lists available at ScienceDirect

Journal of Sound and Vibration

journal homepage: www.elsevier.com/locate/jsvi

Axial and torsional self-excited vibrations of a distributed drill-string

Ulf Jakob F. Aarsnes [a,*], Nathan van de Wouw [b,c,d]

[a] International Research Institute of Stavanger, Forskningsparken AS, Gaustadalléen 21, NO-0349, Oslo, Norway
[b] Eindhoven University of Technology, Department of Mechanical Engineering, Eindhoven, the Netherlands
[c] Department of Civil, Environmental & Geo-Engineering, University of Minnesota, Minneapolis, USA
[d] Delft Center for Systems and Control, Delft University of Technology, Delft, the Netherlands

ARTICLE INFO

Article history:
Received 23 February 2018
Revised 16 October 2018
Accepted 22 December 2018
Available online 28 December 2018
Handling Editor: Ivana Kovacic

Keywords:
Drill-string vibrations
Stick-slip
Distributed parameter systems
Infinite dimensional systems
Stability
Hyperbolic systems

ABSTRACT

We consider a distributed axial-torsional drill-string model with a rate-independent bit-rock interaction law to study the occurrence and non-local characteristics of axial and torsional self-excited vibrations as caused by the regenerative effect. A first contribution of the paper is the derivation of a non-dimensional version of the full non-linear distributed drill-string–bit-rock interaction model and showing how it relates to the minimal set of characteristic quantities. Using this model the study shows how multiple axial modes of the drill-string are excited, or attenuated, depending on the bit rotation rate. This indicates that a lumped drill-string model approximation is insufficient for the general case. Then, a comprehensive simulation study is performed to create a stability map for the occurrence of stick-slip oscillations. In particular, the significance of the axial topside boundary condition, i.e., constant velocity vs. constant hook-load, is evaluated. A central finding is that increasing the axial loop gain (determined by the bit-rock parameters) tends to both increase the area of stable torsional dynamics and increase the rate of penetration for a constant imposed weight on bit. This also corresponds to a more severe axial instability.

1. Introduction

The performance of rotary drilling systems used to drill boreholes in the earth's crust is often limited by the occurrence of self-excited vibrations. Self-excited vibrations cause early fatigue of drill pipes and premature failure of bits and, therefore, should be avoided. Through a combination of damage to equipment, and increased downtime, drill-string vibrations have been reported to account for 2–10% of well costs [1]. As fixed cutter bits (also known as PDC bits) are especially prone to self-excited vibrations, drilling systems employing these bits have seen significant scrutiny and attempts at mitigation of these vibrations.

The dynamics of axial and torsional drill-string vibrations are typically characterized by one or more dominating unstable axial modes causing a standing axial limit-cycle [2–4]. Due to the high gain of the axial feedback loop (related to the interaction of the drill-string dynamics and the rock-cutting process at the bit) causing this instability, removing the axial instability through design or active control is unfeasible in many cases [5]. The most destructive part of the vibrations, however, is often the torsional vibrations of the drill-string, which commonly manifests as a torsional stick-slip limit cycle. Consequently, an approach that has

* Corresponding author.
E-mail addresses: ulaa@norceresearch.no (U.J.F. Aarsnes), n.v.d.wouw@tue.nl (N. van de Wouw).

https://doi.org/10.1016/j.jsv.2018.12.028
0022-460X/

been taken up e.g. in Ref. [6] is to accept the axial instability and instead focus on removing (by the control) the torsional instability or attenuate the severity of the resulting torsional limit cycle.

The stability of the local dynamics of a distributed drill-string (around nominal constant axial and torsional velocity) has been analyzed in previous publications [5,7,8] using linearized models. This approach suffers from the limitation of only determining stability properties of the nominal solution, without assessing the non-local dynamics in case of instability. For most practically relevant drilling conditions the axial dynamics are unstable [2,5] and hence it is of significant practical interest to pursue such a *non-local* analysis. Consequently, in the present work, we consider the full non-linear distributed dynamics of the system. A particular focus is put on how the potential occurrence of torsional stick-slip oscillations is affected by an axial instability of different severity level.

On the one hand, previous work on lumped-parameter models for drilling systems including a regenerative bit-rock-interaction model has shown that axial instabilities lead to axial oscillations [3,9–11]. These axial oscillations induce, in an averaged sense, a velocity-weakening effect of the torque-on-bit with respect to angular bit velocity. In turn, this effect is shown to be the root cause for a torsional instability leading to torsional stick-slip limit cycling, which is highly undesired in practice. On the other hand, it has been shown recently in Refs. [5,7,8], that the distributed dynamics of the drill-string can significantly affect the local stability properties of the system. Given the fact that both the lumped-parameter and distributed models show that an axial instability is unavoidable in most practical cases, a non-local analysis of both the axial dynamics and the coupled axial-torsional dynamics is needed. Such an analysis should shed light on whether the mechanism wherein non-local axial dynamics can induce a torsional instability in lumped-parameter models, also holds for the distributed model. This problem has not been addressed in the literature and is the central focus of this paper.

In the present paper, we undertake a structured simulation study of the full non-linear distributed dynamics of drill-string–bit-rock interaction system. We start the study by considering the axial dynamics, uncoupled from the torsional dynamics, by assuming a constant angular velocity. This enables us to investigate, firstly, the axial quasi limit-cycle, resulting from an axial instability, secondly, how it changes with different angular bit velocity and, thirdly, the severity of the axial instability. It also enables the evaluation of the 'apparent velocity weakening effect' in the torque-on-bit as influenced by the axial limit cycle (as observed in Refs. [3,9] for lumped-parameter models). Next we consider the full, coupled axial–torsional, dynamics and evaluate the impact of changing the system parameters on the occurrence of a torsional stick-slip limit-cycle.

Contributions of this paper include, firstly, deriving a non-dimensional version of the full non-linear distributed drill-string–bit-rock interaction model and show how it relates to the *minimal set of characteristic quantities* derived in Ref. [5]. Secondly, we present a simulation study of the axial limit-cycle of the distributed drill-string model which enables comparison with the results of lumped-parameter models in Refs. [3,4,9,10,12–14]. Thirdly, we investigate and map the occurrence of torsional stick-slip vibration in the coupled, distributed, non-linear model as parametrized in the system parameters. Finally, several conclusions are drawn based on this analysis, which significantly enhance the understanding of coupled self-excited vibrations in a distributed drill string.

2. Model description

This section derives the mathematical description of the non-local dynamics of the drilling system depicted in Fig. 1. First, we introduce the distributed axial–torsional drill-string dynamics in Section 2.1. Second, the axial–torsional dynamics are coupled through a non-linear bit–rock interaction law described as a transport equation in Section 2.2.

2.1. Distributed drill-string model

We use the distributed drill-string model as derived in Refs. [2,5,7]. As in these previous models there is no axial-torsional coupling along the drill string. This is an approximation required to facilitate the analysis performed in the paper. We denote the axial velocity and force by $v(t,x)$, $w(t,x)$, respectively, where $(t,x) \in [0,\infty) \times [0,L]$, with L the length of the drill-string. The axial force can be found from the strain, given as the local relative compression $w(t,x) = AE\left(\xi(t,x) - \xi(t,x+dx)\right)/dx$, where $\xi(t,x)$ is the axial displacement such that $\frac{\partial \xi(t,x)}{\partial t} = v(t,x)$, and $dx \to 0$ is an infinitesimal axial position increment, A is the cross-sectional area of the element and E is the Young's modulus. Further, ρ is the pipe mass density and k_a is a damping coefficient accounting for viscous dissipation. Then, the axial motion is governed by the following partial differential equations:

$$\frac{\partial w(t,x)}{\partial t} + AE\frac{\partial v(t,x)}{\partial x} = 0 \tag{1}$$

$$A\rho\frac{\partial v(t,x)}{\partial t} + \frac{\partial w(t,x)}{\partial x} = -k_a \rho A v(t,x). \tag{2}$$

Equivalently, for the angular motion, we denote the angular velocity and torque as $\omega(t,x), \tau(t,x)$, respectively, with $(t,x) \in [0,\infty) \times [0,L]$. The torque is found from shear strain, given as twist per unit length, and letting ϕ denote the angular displacement in the string such that $\frac{\partial \phi(t,x)}{\partial t} = \omega(t,x)$, we have $\tau(t,x) = JG\left(\phi(t,x) - \phi(t,x+dx)\right)/dx$. Here J is the polar moment

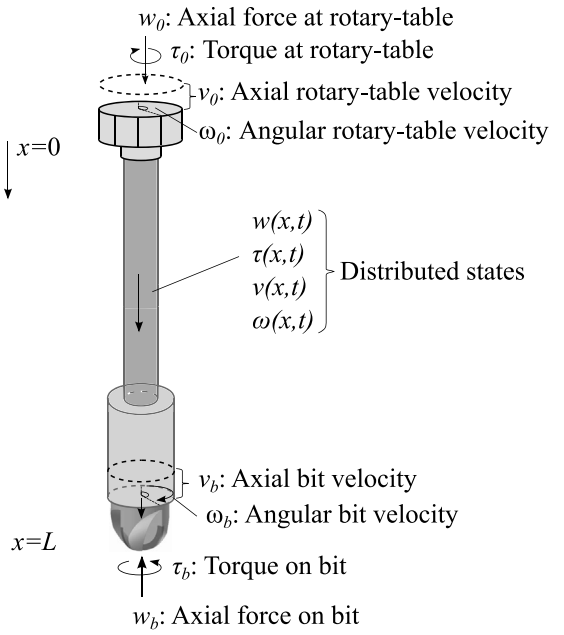

Fig. 1. Schematic of the drill-string system under consideration.

for inertia and G is the shear modulus. Hence, the angular motion is governed by the following partial differential equations:

$$\frac{\partial \tau(t,x)}{\partial t} + JG\frac{\partial \omega(t,x)}{\partial x} = 0 \tag{3}$$

$$J\rho\frac{\partial \omega(t,x)}{\partial t} + \frac{\partial \tau(t,x)}{\partial x} = -k_t\rho J\omega(t,x), \tag{4}$$

where k_t is a damping coefficient representing the shear stresses between the pipe and drilling mud.

The drill-string is coupled with the bit-rock interaction at the boundary through the right-side (downhole) boundary condition

$$w(t,x=L) = w_b, \qquad \tau(t,x=L) = \tau_b \tag{5}$$

with w_b the weight (force) on bit and τ_b the torque on bit, while at the left boundary (topside) the torsional boundary condition is given by a specified top drive velocity

$$\omega(t,x=0) = \omega_0. \tag{6}$$

For the axial topside boundary, we consider two different boundary conditions: using either constant axial velocity (7) *or* constant hook-load (8), given, respectively, by

$$v(t,x=0) = v_0, \tag{7}$$

$$w(t,x=0) = w_0. \tag{8}$$

The bit–rock interaction determining w_b and τ_b in (5) is described next.

2.2. Bit-rock interaction law

We use the bit-rock interaction law of [15], but in the equivalent reformulation as a transport equation description due to Refs. [13,14]. This description is reiterated here concisely for completeness.

Let the independent variable $\theta \in [0,1]$ denote the normalized angle between a point at the bit to a cutter at the bit, such that $\theta = 0$ is at a cutter and $\theta = 1$ is at the next cutter blade, see Fig. 2. The variable $\lambda(t,\theta)$ then represents the depth of uncut rock at position θ relative to the axial bit position. That is $\lambda(t,0) = 0$, at (after) a cutting blade, and consequently the depth of $d(t)$ at the following blade is given as $d(t) = \lambda(t,1)$. The evolution of λ can be described by the transport equation

$$\frac{\partial \lambda(t,\theta)}{\partial t} + \omega_b(t)\frac{N}{2\pi}\frac{\partial \lambda(t,\theta)}{\partial \theta} = v_b(t), \tag{9}$$

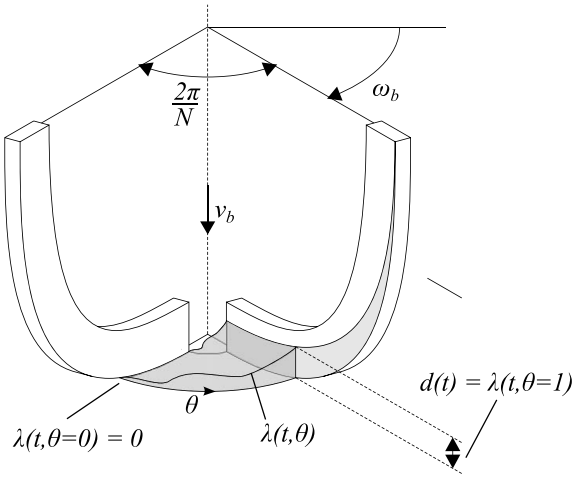

Fig. 2. Bit rock interaction.

where v_b, ω_b are the axial and angular bit velocities, respectively, and N is the number of cutter blades. We refer to Refs. [13,14] for the full derivation.

Following [15], the weight on bit is given as

$$w_b = a\zeta\epsilon Nd + w_f g(v_b), \tag{10}$$

where the $a\zeta\epsilon Nd$ term is due to the cutting force with a the bit radius, ζ is a cutter sharpness coefficient and ϵ the rock intrinsic specific energy. The second term, $w_f g(v_b)$, denotes the wearflat force component where w_f is the normal force that must be overcome before axial cutting is initiated, while non-linear function $g(v_b)$ (colloquially referred to as the $g(\cdot)$ non-linearity) is a set-valued map described as (following the description of [9]):

$$g(v_b) = \frac{1 - \mathrm{Sign}(v_b)}{2} = \begin{cases} 0, & v_b < 0 \\ [0,1], & v_b = 0 \\ 1, & v_b > 0 \end{cases}, \tag{11}$$

where $\mathrm{Sign}(\cdot)$ is the set-valued sign function. Similarly for the torque on bit, we have

$$\tau_b = a^2\epsilon Nd + \tau_f \widetilde{g}(\omega_b), \tag{12}$$

where $\widetilde{g}(\omega_b)$ enforce torsional stick if the torque applied to the bit by the drill-string can not overcome the torque induced by the bit-rock interaction. If it is higher then that torque-on-bit, then the bit starts to slip torsionally. I.e.,

$$\widetilde{g}(\omega_b) = \frac{1 - \mathrm{Sign}(\omega_b)}{2} = \begin{cases} 0, & \omega_b < 0 \\ [0, g(v_b)], & \omega_b = 0 \\ 1, & \omega_b > 0 \end{cases}. \tag{13}$$

3. Dimensionless model formulation

To support the subsequent analysis and simulation study, we will non-dimensionalize the system model in such a way as to express it in a small number of dimensionless parameters derived from the characteristic quantities of the physical system. The associated detailed derivations are given in Appendix A.

3.1. Variables and parameters definitions

The independent variables of the model are rendered dimensionless as follows: $\overline{t} = \frac{t}{t_t} = t\frac{c_t}{L}, \overline{x} = \frac{x}{L}$, where c_t is the torsional wave velocity.

Dependent variables of the model are rendered dimensionless as follows: $V = \frac{v}{v^*}, W = \frac{w}{w^*}, \Omega = \frac{\omega}{\omega^*}, T = \frac{\tau}{\tau^*}, \Lambda = \frac{\lambda}{d^*}$.

Characteristic quantities used for non-dimensionalization are given by

$$v^* = \frac{d^*}{t_t} = \frac{2\pi JG}{LNt_t} = \frac{JG2\pi}{a^2\epsilon N^2 L t_t} \tag{14}$$

$$w^* = \frac{AEd^*}{L} = \frac{JGAE2\pi}{a^2\epsilon N^2 L^2} \tag{15}$$

$$\omega^* = \frac{2\pi}{Nt_t} \tag{16}$$

$$\tau^* = \frac{JG\omega^* t_t}{L} = \frac{JG2\pi}{NL} \tag{17}$$

$$d^* = \frac{\tau^*}{a^2\epsilon N} = \frac{JG2\pi}{a^2\epsilon N^2 L}. \tag{18}$$

See Appendix A for a physical interpretation of these quantities.

Dimensionless parameters characterizing the model in Section 3.2 are then given by $\overline{k}_a = k_a t_t, \overline{k}_t = k_t t_t, \overline{c} = \frac{c_a}{c_t}$, and

$$K_a = \overline{c}\frac{a\zeta\epsilon L}{EA}N, \qquad K_t = \frac{v_0}{\omega_0}a^2\epsilon N\frac{L}{JG}. \tag{19}$$

Here $\overline{k}_t, \overline{k}_a$ determines the in-domain damping of the system, $\overline{c}$ the relative axial to torsional wave velocity, and K_a, K_t are the axial and torsional nominal loop gains, respectively, as defined in Ref. [5].

3.2. Dimensionless PDE model

Expressed in the non-dimensional variables, the system dynamics are described as follows. The depth-of-cut, Λ, is described by the transport equation

$$\frac{\partial\Lambda(\overline{t},\theta)}{\partial\overline{t}} + \Omega_b(\overline{t})\frac{\partial\Lambda(\overline{t},\theta)}{\partial\theta} = V_b(\overline{t}), \tag{20}$$

where

$$\Lambda(\overline{t},\theta=0) = 0, \qquad D(\overline{t}) = \Lambda(\overline{t},1). \tag{21}$$

This is used to express the weight- and torque-on-bit as follows:

$$W_b(\overline{t}) = \frac{K_a}{\overline{c}}D(\overline{t}) + W_f g(V_b), \quad W_f := \frac{w_f}{w^*}, \tag{22}$$

$$T_b(\overline{t}) = D(\overline{t}) + \beta W_f g(V_b), \quad \beta := \frac{\tau_f}{\tau^*}\frac{w^*}{w_f}. \tag{23}$$

Note the definition of β in (23), which is called the bit-rock interaction number in Ref. [4]. β relates the magnitude of changes in the axial wearflat force to changes in the wearflat torque. That is, a large β means that activation of the $g(\cdot)$ nonlinearity has a large effect on the torque on bit. Consequently, it determines to what degree the wearflat forces influence the torsional dynamics (and the potential occurrence of stick slip oscillations). The dimensionless axial drill-string dynamics are given by

$$\frac{\partial W(\overline{t},\overline{x})}{\partial\overline{t}} + \frac{\partial V(\overline{t},\overline{x})}{\partial\overline{x}} = 0 \tag{24}$$

$$\frac{\partial V(\overline{t},\overline{x})}{\partial\overline{t}} + \overline{c}^2\frac{\partial W(\overline{t},\overline{x})}{\partial\overline{x}} = -\overline{k}_a V(t,x), \tag{25}$$

with the downhole boundary condition

$$W(\overline{t},\overline{x}=L) = w_b(\overline{t})\frac{L}{AEd^*} = W_b(\overline{t}), \tag{26}$$

while at the topside we use either (27) *or* (28):

$$V(\overline{t},\overline{x}=0) = v_0\frac{t_t}{d^*} = V_0 \tag{27}$$

$$W(\overline{t},\overline{x}=0) = w_0\frac{L}{AEd^*} = W_0, \tag{28}$$

reflecting an imposed axial velocity (rate of penetration), or imposed axial force (hook-load), boundary condition, respectively. The dimensionless torsional drill-string dynamics are given by

$$\frac{\partial T(\bar{t},\bar{x})}{\partial \bar{t}} + \frac{\partial \Omega(\bar{t},\bar{x})}{\partial \bar{x}} = 0 \tag{29}$$

$$\frac{\partial \Omega(\bar{t},\bar{x})}{\partial \bar{t}} + \frac{\partial T(\bar{t},\bar{x})}{\partial \bar{x}} = -\bar{k}_t \omega(t,x), \tag{30}$$

with respectively topside and downhole boundary conditions given by

$$\Omega(\bar{t},\bar{x}=0) = \omega_0 \frac{Nt_t}{2\pi} \coloneqq \Omega_0 \tag{31}$$

$$T(\bar{t},\bar{x}=L) = \tau_b(\bar{t}) \frac{LN}{JG2\pi} \coloneqq T_b(\bar{t}). \tag{32}$$

3.3. Steady-state solution

Assuming $\Omega_0 > 0$ and $V_0 > 0$ or $W_0 > W_f$, the steady-state-solution is unique and is derived below. Denoting the steady-state solution with an overbar symbol, we note that $\overline{\Omega}(\bar{x}) = \Omega_0, \forall \bar{x} \in [0,1]$ and $\overline{V}(\bar{x}) = V_0, \forall \bar{x} \in [0,L]$ for the top-side boundary condition in (27). For the case of the boundary condition in (28) $\overline{V}$ can be found from W_0, as will be shown later. The steady-state cuttings profile can be found from (20):

$$\overline{\Lambda}(\theta) = \frac{\overline{V}}{\overline{\Omega}}\theta. \tag{33}$$

Consequently, the steady-state depth of cut is given by $\overline{D} = \overline{\Lambda}(1) = \frac{\overline{V}}{\overline{\Omega}}$, and thus from (22), (23) we obtain the steady-state weight and torque on bit:

$$\overline{W}_b = \frac{K_a}{\bar{c}} \frac{\overline{V}}{\overline{\Omega}} + W_f, \tag{34}$$

$$\overline{T}_b = \frac{\overline{V}}{\overline{\Omega}} + \beta W_f. \tag{35}$$

For the axial drill-string dynamics, we obtain from (25) the steady state axial force:

$$\overline{W}(\bar{x}) = \overline{W}_b + \frac{1}{\bar{c}^2} \bar{k}_a \overline{V}(1-\bar{x}), \tag{36}$$

and similarly for the torsional drill-string dynamics the torque satisfies, from (30),

$$\overline{T}(\bar{x}) = \overline{T}_b + \bar{k}_t \overline{\Omega}(1-\bar{x}). \tag{37}$$

For the case of constant hook-load, i.e. when using the top-side boundary condition in (28), $\overline{V}$ must be computed from the specified hook-load W_0. We have from (34) and (36):

$$\overline{V} = \frac{1}{\frac{\bar{k}_a}{\bar{c}^2} + \frac{K_a}{\bar{c}} \frac{1}{\overline{\Omega}}} \left(W_0 - W_f\right). \tag{38}$$

3.4. Numerical implementation

In the numerical implementation of the model, the wave equations (24), (25) and (29), (30), are transformed into their Riemann invariants [16] and all the five resulting transport equations of the system, including (20), are then solved with a first-order upwind scheme [17]. This was done to avoid spurious oscillations, as it was found that higher-order schemes performed poorly due to the temporal discontinuities introduced by the differential inclusion nature of the model induced by the bit rock interaction model in Section 2.2. For reference, the algorithm runs at a speed of roughly 10 dimensionless time units per second.

In all simulations, a spatial grid of 2000 cells was used for the drill-string and the time-step was chosen so as to enforce a Courant number of approximately 0.9, thus satisfying the Courant–Friedrichs–Lewy (CFL) condition [18]. The cell number for (20) was then chosen such that the CFL condition was enforced for a bit angular velocity of five times the nominal, i.e., $\Omega_b < 5\Omega_0$ was assumed.

4. Linearized model description in the Laplace domain

In this section, we derive the model description in the Laplace domain from the dimensionless model formulation from Section 3. This model description is pursued to show how the non-linear model relates to the linearized model studied in Refs. [5,7]. The corresponding stability results therein will be used to interpret the simulation results presented in the following. To obtain the Laplace domain model description we cast the model in perturbation variables, i.e., in deviations from the steady state derived in Section 3.3, and derive the linearized version of the bit rock interaction law of Section 2.2. This model linearization can also be found in Refs. [5,7]. We then perform the Laplace transform and show that the result conforms with existing descriptions in the literature.

We let the superscripts 'overbar' and 'tilde' denote the steady-state solution and the deviation from this steady-state solution, respectively, for a given variable.

4.1. Drill-string

As was derived in Refs. [5,7] and restated in Appendix C, we can characterize the linearized drill-string dynamics by transfer functions. Using the Laplace variable $s \in \mathbb{C}$ as the argument to indicate variables in the Laplace domain, we have, for the torsional drill-string dynamics:

$$\frac{\widetilde{\Omega}_b}{\widetilde{T}_b}(s) = -g_t(s), \quad g_t(s) = \frac{\tanh\left(s\sqrt{1+\frac{\overline{k}_t}{s}}\right)}{\sqrt{1+\frac{\overline{k}_t}{s}}}, \tag{39}$$

Note that the Laplace transform is performed from the time-domain to the s-domain. Similarly, for the axial dynamics,

$$\frac{\widetilde{V}_b}{\widetilde{W}_b}(s) = -\overline{c}g_a(s), \tag{40}$$

where the transfer function $g_a(s)$ depends on the topside boundary condition (BC):

$$g_a(s) = \begin{cases} \dfrac{\tanh\left(\frac{s}{\overline{c}}\sqrt{1+\frac{\overline{k}_a}{s}}\right)}{\sqrt{1+\frac{\overline{k}_a}{s}}}, & \text{for BC (27).} \\ \dfrac{1}{\sqrt{1+\frac{\overline{k}_a}{s}}\tanh\left(\frac{s}{\overline{c}}\sqrt{1+\frac{\overline{k}_a}{s}}\right)}, & \text{for BC (28).} \end{cases} \tag{41}$$

Here we recall that BC (27) corresponds to constant imposed topside axial velocity, while BC (28) corresponds to constant hook-load.

4.2. Bit rock interaction law

We now show that the linearized version of (9) is equivalent to the linearized delay equations used in the RGD model [10] to describe the depth-of-cut as a function of (delayed) axial motion.

Let the superscripts 'overbar' and 'tilde' denote the steady-state solution and the deviation from this steady-state solution, respectively, for a given variable. E.g., for the depth of cut profile we have $\widetilde{\Lambda}(\theta,\bar{t}) = \Lambda(\theta,\bar{t}) - \overline{\Lambda}(\theta)$.

Linearizing (20) around the steady-state profile $\overline{\Lambda}(\theta)$ we obtain

$$\frac{\partial\widetilde{\Lambda}(\bar{t},\theta)}{\partial\bar{t}} + \left(\widetilde{\Omega}_b(\bar{t})\frac{\partial\overline{\Lambda}(\theta)}{\partial\theta} + \overline{\Omega}\frac{\partial\widetilde{\Lambda}(t,\theta)}{\partial\theta}\right) = \widetilde{V}_b(\bar{t}). \tag{42}$$

The steady-state gradient of $\overline{\Lambda}(\theta)$ is given by the steady-state velocities $\overline{\Omega}, \overline{V}$ from (33) as follows:

$$\frac{\partial\overline{\Lambda}(\theta)}{\partial\theta} = \frac{\overline{V}}{\overline{\Omega}}. \tag{43}$$

Taking the Laplace Transform of (42) while using (43),

$$\widetilde{\Lambda}(s,\theta)s + \left(\widetilde{\Omega}_b(s)\frac{\overline{V}}{\overline{\Omega}} + \overline{\Omega}\frac{\partial\widetilde{\Lambda}(s,\theta)}{\partial\theta}\right) = \widetilde{V}_b(s). \tag{44}$$

Hence, we obtain

$$\frac{\partial \widetilde{\Lambda}(s,\theta)}{\partial \theta} = \frac{1}{\overline{\Omega}}\left(\widetilde{V}_b(s) - \widetilde{\Lambda}(s,\theta)s - \widetilde{\Omega}_b(s)\frac{\overline{V}}{\overline{\Omega}}\right), \tag{45}$$

$$\widetilde{\Lambda}(s,0) = 0. \tag{46}$$

Note that (45) is a linear ODE in θ with initial condition (46), which we can solve to obtain

$$\widetilde{\Lambda}(s,\theta) = C_1 \mathrm{e}^{-\theta s/\overline{\Omega}} + \frac{1}{s}\left(\widetilde{V}_b(s) - \widetilde{\Omega}_b(s)\frac{\overline{V}}{\overline{\Omega}}\right), \tag{47}$$

where C_1 is an integration constant. Enforcing (46)

$$\widetilde{\Lambda}(s,0) = C_1 + \frac{1}{s}\left(\widetilde{V}_b(s) - \widetilde{\Omega}_b(s)\frac{\overline{V}}{\overline{\Omega}}\right) = 0 \tag{48}$$

$$\implies C_1 = -\frac{1}{s}\left(\widetilde{V}_b(s) - \widetilde{\Omega}_b(s)\frac{\overline{V}}{\overline{\Omega}}\right). \tag{49}$$

Hence we find the Laplace transformed linearized depth of cut as

$$\widetilde{D}(s) = \widetilde{\Lambda}(s,1) = \frac{1}{s}\left(\widetilde{V}_b(s) - \widetilde{\Omega}_b(s)\frac{\overline{V}}{\overline{\Omega}}\right)\left(1 - \mathrm{e}^{-s/\overline{\Omega}}\right), \tag{50}$$

and from (22), (23) (noting that the $g(\cdot)$ nonlinearities disappear in the linearized perturbation variables) we obtain:

$$\widetilde{W}_b(s) = \frac{K_a}{\overline{c}}\widetilde{D}(s), \qquad \widetilde{T}_b(s) = \widetilde{D}(s), \tag{51}$$

which is consistent with the expressions used in Refs. [7,10,12,19].

4.3. Characteristic function

Combining (39), (40) and (50), (51) we obtain the feedback loop generated by the regenerative effect of the rock-cutting process interacting with the drill-string dynamics, the stability of which can be determined by applying the Nyquist criterion to the characteristic equation [7]:

$$0 = G(s) + 1 \tag{52}$$

$$G(s) = G_a(s) + G_t(s) \tag{53}$$

$$G_a(s) = g_a(s)\frac{K_a}{s}\left(1 - \mathrm{e}^{-s/\Omega_0}\right) \tag{54}$$

$$G_t(s) = -g_t(s)\frac{K_t}{s}\left(1 - \mathrm{e}^{-s/\Omega_0}\right), \tag{55}$$

where key quantities are the axial and torsional loop gain parameters, K_a, K_t, given as

$$K_a = \frac{\overline{c}a\zeta\epsilon NL}{EA} \tag{56}$$

$$K_t = \frac{\overline{V}}{\overline{\Omega}}. \tag{57}$$

The Nyquist criterion predicts instability if the Nyquist contour of the characteristic function $G(s)$ encircles -1. In the uncoupled case considered in Section 5, $G_t(s) = 0$ and Nyquist criterion can be checked by considering the phase and magnitude of $G_a(s)$. We refer to Refs. [5,7] for details on this kind of analysis. Note that the torsional loop gain K_t is dependent on the steady-state axial velocity $\overline{V}$. For the case of imposed axial topside velocity, (27), we have $K_t = \frac{v_0}{\omega_0}\frac{t_t}{d^*}\frac{2\pi}{Nt_t} = \frac{v_0}{\omega_0}a^2\epsilon N\frac{L}{JG}$ which can be shown to be consistent with [5,7].

Remark 1. *Note the appearance of the relative wave velocity, $\overline{c}$, in the axial loop gain K_a in (56), which is due to the frequency variable having been normalized with the torsional wave travel time, t_t, and not with the axial one.*

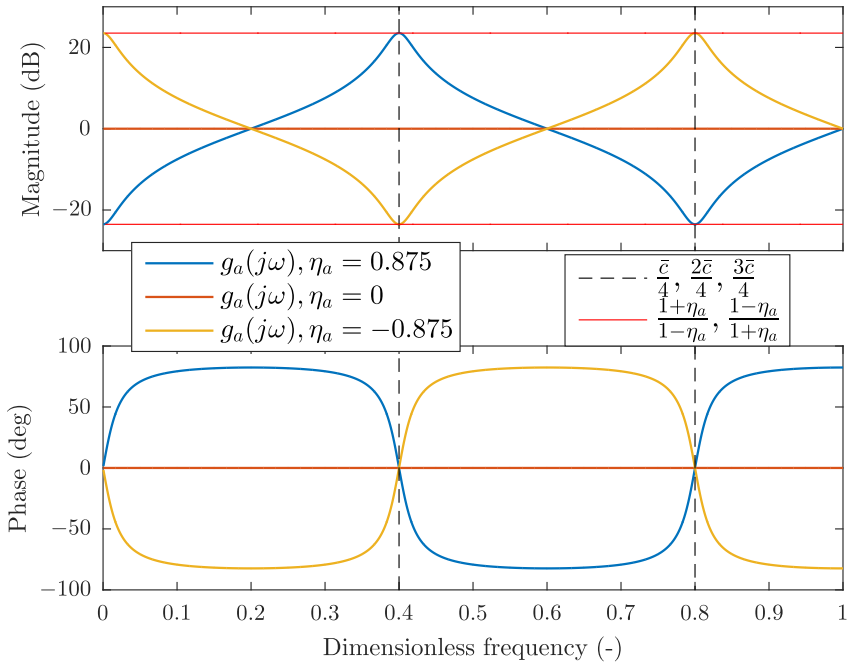

Fig. 3. The frequency response function $g_a(j\omega)$ of the input-output description of the axial dynamics of a distributed drill-string.

5. Global dynamic analysis of the uncoupled axial dynamics

The rest of the paper is dedicated to dynamic analysis with the derived dimensionless model. To structure the analysis, we start by considering the uncoupled axial dynamics. Such an approach has been pursued previously for lumped models [2,9] and the goal is to enable the derivation of an averaged torque on bit for a given angular bit velocity. The uncoupling greatly reduces the complexity of the dynamics which facilitates analysis. Furthermore, in the mentioned literature on lumped models, such a decoupling is motivated by a time-scale separation between the axial and torsional limit-cycles. However, as we will see in the following, this time-scale separation is not always valid for the distributed dynamics considered here.

Recall that the coupling between the axial and torsional drill-string dynamics are due to the bit rock interaction: the uncoupled axial model is obtained by setting the angular velocity of the bit in (20) to be fixed (i.e., $\Omega_b = \Omega_0$). Section 5 is *not* required to follow Section 6, so the reader can choose to skip ahead. The main conclusions are summarized at the end of the section.

5.1. Axial distributed drill-string

The non-dimensional axial dynamics of the distributed drill-string, given by (24)–(25), can be described by the input-output relation between the weight on bit, W_b, and bit velocity, V_b, as given by (40). This function is specified by the parameters $\overline{c}$ and $\overline{k}_a$. The damping $\overline{k}_a$ can also be specified by the pseudo reflection coefficient η_a, given by

$$\eta_a = \begin{cases} e^{-2\frac{\overline{k}_a}{\overline{c}}}, & \text{for BC (27).} \\ -e^{-2\frac{\overline{k}_a}{\overline{c}}}, & \text{for BC (28).} \end{cases} \tag{58}$$

such that $\eta_a \in [-1, 1]$ and $|\eta_a| = 1$ indicates no damping, while a small $|\eta_a|$ indicates high damping, see Ref. [5]. The effect of these parameters is illustrated in the frequency domain in Fig. 3 and in the time domain in Fig. 4. In these figures we see that the dimensionless drill-string response exhibits resonances with a period given by $\overline{c}$ and with a magnitude given by η_a.

5.2. Axial limit cycle of the distributed axial system

The axial transfer function, $g_a(s)$, enters in the characteristic equation of the axial dynamics (54):

$$G_a(s) = g_a(s)\frac{K_a}{s}(1 - e^{-s/\Omega_0}). \tag{59}$$

Local stability properties of the axial dynamics can be determined from (59) according to the conditions derived in Ref. [7], and a stability map parametrized in the characteristic quantities $K_a, \eta_a, \overline{\Omega}$ was presented in Ref. [5]. Recall from Ref. [5] that for

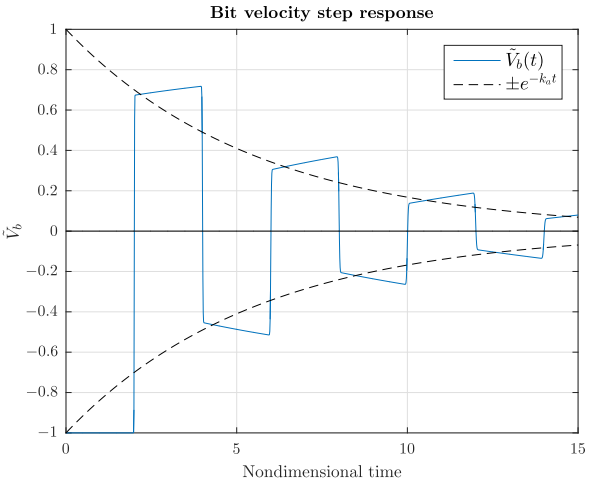

Fig. 4. Step response of the linear infinite-dimensional axial drill string described by the frequency response function $g_a(s)$.

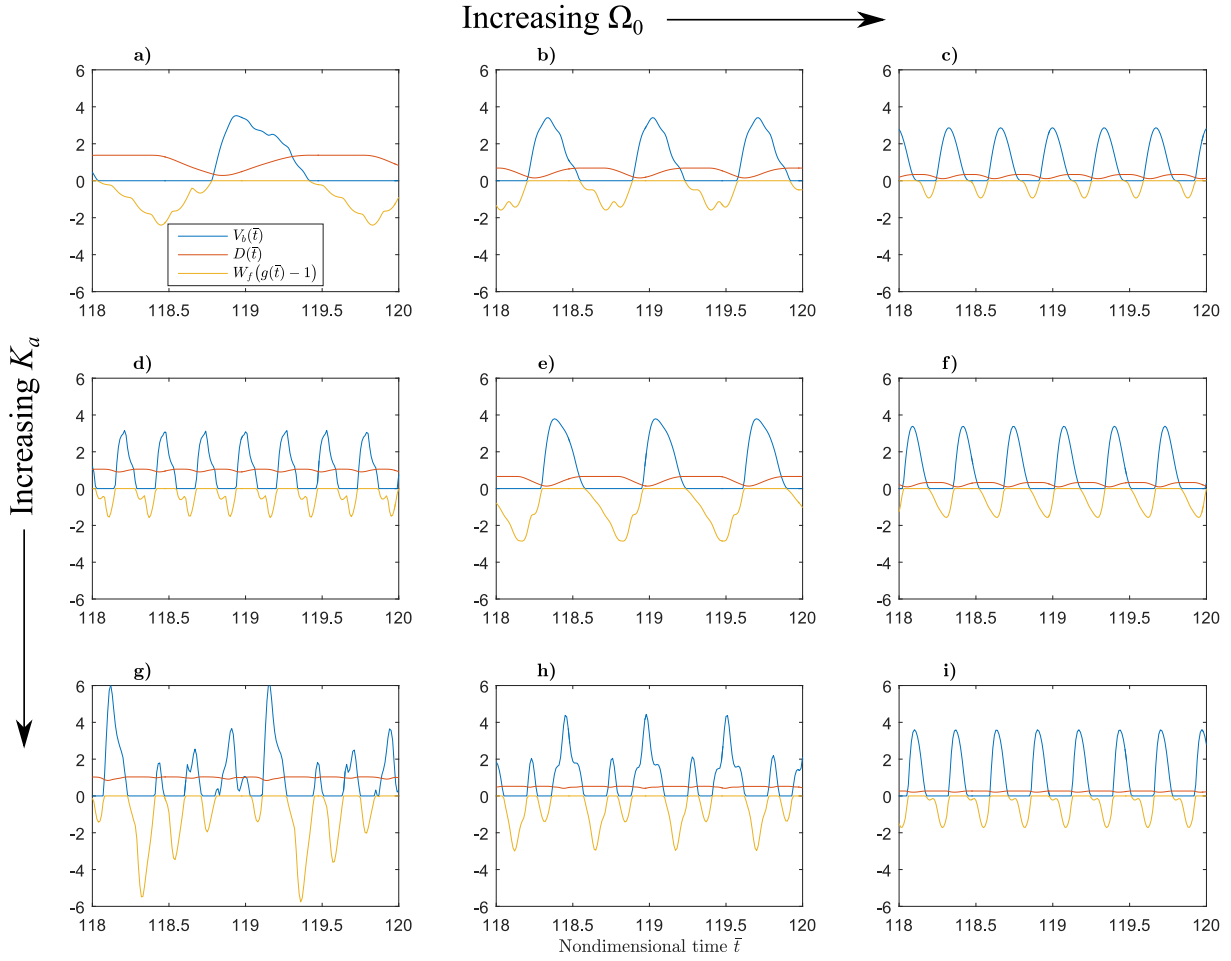

Fig. 5. Axial "limit cycles" (axial velocity $V_b(\bar{t})$, depth of cut $D(\bar{t})$ and the changes in the wear-flat force component $\beta(g(\bar{t})-1)$ to the weight on bit) for different rotation rates Ω_0 and axial gains K_a with constant axial top-drive velocity: $V_0 = 1$, BC (7), $\bar{c} = 1.6$ and pseudo reflection coefficient $\eta_a = 0.7$. The rotation rates and axial gains are; **a)** $\Omega_0 = 1, K_a = 10$, **b)** $\Omega_0 = 2, K_a = 10$, **c)** $\Omega_0 = 4, K_a = 10$, **d)** $\Omega_0 = 1, K_a = 20$, **e)** $\Omega_0 = 2, K_a = 20$, **f)** $\Omega_0 = 4, K_a = 20$, **g)** $\Omega_0 = 1, K_a = 40$, **h)** $\Omega_0 = 2, K_a = 40$, **i)** $\Omega_0 = 4, K_a = 40$.

Table 1
Table of unstable modes of parameter sets with constant axial top-drive velocity, simulated in Fig. 5.

Case	Parameters			Four *most* unstable modes							
#	Ω_0	K_a	η_a	$K_aM_{G,a}$	freq.	$K_aM_{G,a}$	freq.	$K_aM_{G,a}$	freq.	$K_aM_{G,a}$	freq.
a)	1	10	0.7	5.81	0.58	4.66	2.82	3.09	3.66	1.92	6.82
b)	2	10	0.7	7.55	1.27	3.64	3.62	1.87	5.27	1.72	7.62
c)	4	10	0.7	4.76	2.84	2.26	3.61	1.97	6.84	1.24	10.8
d)	1	20	0.7	11.6	0.58	9.32	2.82	6.17	3.66	3.83	6.82
e)	2	20	0.7	15.1	1.27	7.29	3.62	3.74	5.27	3.44	7.62
f)	4	20	0.7	9.53	2.84	4.52	3.61	3.94	6.84	2.47	10.8
g)	1	40	0.7	23.3	0.85	18.6	2.82	12.3	3.66	7.67	6.82
h)	2	40	0.7	30.2	1.27	14.6	3.62	7.48	5.27	6.89	7.62
i)	4	40	0.7	19.1	2.84	9.05	3.61	7.88	6.84	4.94	10.8

given $\eta_a, \overline{\Omega}$, a normalized inverse gain margin $M_{G,a}$ can be derived which indicates the loop gain K_a required to make the system unstable: where $K_aM_{G,a} > 1$ (i.e. 0 dB) indicates instability of the uncoupled axial dynamics. In the following exposition, we will use these quantities in the analysis to indicate the degree of instability. Moreover, we investigate the limit cycles (i.e., non-local dynamics) that occur when the axial steady-state solution is unstable, which is typically the case for realistic parameter sets.

Axial limit cycles for different rotation rates, Ω_0, and axial loop gains, K_a, are show in Fig. 5. In these simulations, a constant angular bit velocity is enforced, i.e., $\Omega_b = \Omega_0$, while the simulations run for 120 (nondimensional time units) to allow an axial

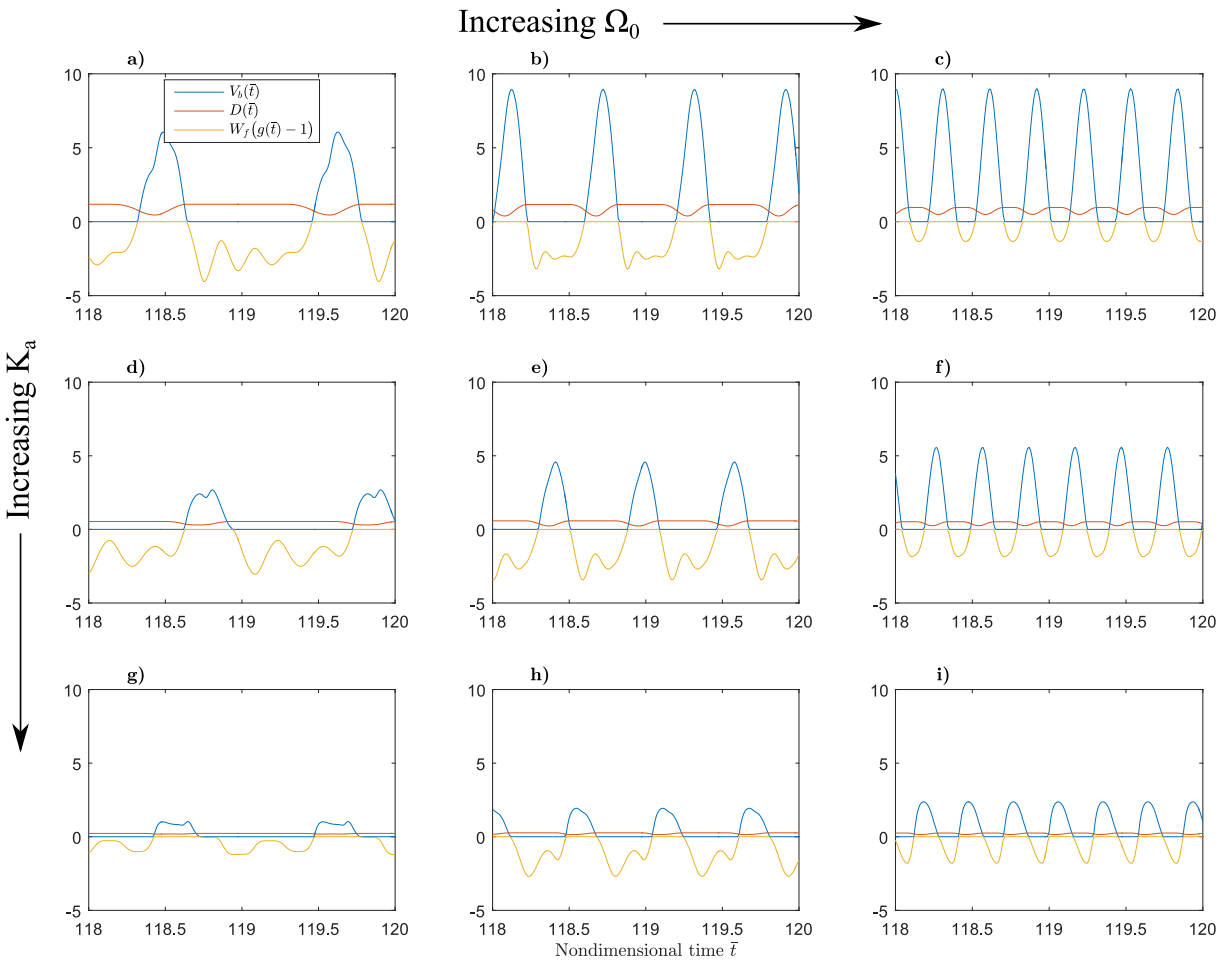

Fig. 6. Axial "limit cycles" (axial velocity $V_b(\bar{t})$, depth of cut $D(\bar{t})$ and the changes in the wear-flat force component $\beta(g(\bar{t})-1)$ to the weight on bit) for different rotation rates Ω_0 and axial gains K_a with constant hook-load: $W_0 - W_f = 5$, BC (8), $\overline{c} = 1.6$ and pseudo reflection coefficient $\eta_a = -0.7$. The rotation rates and axial gains are; **a)** $\Omega_0 = 1, K_a = 10$, **b)** $\Omega_0 = 2, K_a = 10$, **c)** $\Omega_0 = 4, K_a = 10$, **d)** $\Omega_0 = 1, K_a = 20$, **e)** $\Omega_0 = 2, K_a = 20$, **f)** $\Omega_0 = 4, K_a = 20$, **g)** $\Omega_0 = 1, K_a = 40$, **h)** $\Omega_0 = 2, K_a = 40$, **i)** $\Omega_0 = 4, K_a = 40$.

Table 2
Table of unstable modes for parameter sets with constant hook-load, simulated in Fig. 6.

Case	Parameters			Four *most* unstable modes							
#	Ω_0	K_a	η_a	$K_aM_{G,a}$	freq.	$K_aM_{G,a}$	freq.	$K_aM_{G,a}$	freq.	$K_aM_{G,a}$	freq.
a)	1	10	−0.7	15.3	0.82	6.59	1.66	2.72	4.82	1.99	5.66
b)	2	10	−0.7	8.15	1.62	3.02	3.27	2.34	5.62	1.36	9.62
c)	4	10	−0.7	4.19	3.22	3.49	2.48	1.86	7.22	1.36	6.48
d)	1	20	−0.7	30.6	0.82	13.2	1.66	5.44	4.82	3.98	5.66
e)	2	20	−0.7	16.3	1.62	6.04	3.27	4.68	5.62	7.72	9.62
f)	4	20	−0.7	8.38	3.22	6.97	2.48	3.72	7.22	2.76	6.48
g)	1	40	−0.7	61.2	0.82	26.4	1.66	10.9	4.82	7.97	5.66
h)	2	40	−0.7	32.6	1.62	12.1	3.27	9.36	5.62	5.44	9.62
i)	4	40	−0.7	16.8	3.22	13.9	2.48	7.44	7.22	5.46	6.48

quasi limit-cycle to develop. For the topside boundary condition (27) of constant axial velocity, Fig. 5 shows the axial limit cycle for $\bar{t} \in [118, 120]$ of these simulations for the different rotations rates Ω_0 and gains K_a.

A summary of the magnitude and frequency location of the unstable axial modes is given in Table 1. By *most* unstable mode we mean the value $K_aM_{G,a}$ that is associated with the specific mode. Similarly, for the case of the constant hook-load boundary condition, the simulation is shown in Fig. 6 and the unstable axial modes summarized in Table 2. These unstable modes are associated with unstable pairs of eigenvalues of the linearized dynamics, while Figs. 5 and 6 show the non-local axial behavior developing as a consequence of these unstable modes.

It is clear from the simulations that increasing the RPM, Ω_0, increases the frequency of the axial vibrations. This can be seen in Table 1 where the *most* unstable mode is associated with the frequency 0.58 for $\Omega_0 = 1$, but frequencies 1.27 and 2.84 for $\Omega_0 = 2$ and 4, respectively. Similarly for Table 2, the frequency of the most unstable mode increases from 0.82 to 1.62 and 3.22 when Ω_0 is increased from 1 to 2 and 4. This is predicted by the linear stability analysis in Ref. [7] by the criterion that the delay factor (which is given by the angular bit velocity Ω_b) must have a negative phase contribution in the frequency range of an axial instability.

Note the effect of the different boundary conditions, as reflected in differences in Figs. 5 and 6. For a constant imposed axial velocity, the average depth of cut is inversely proportional to the angular velocity, through the relation $\overline{D} = \overline{V}/\overline{\Omega}$. This means that the average depth of cut reduces with increasing angular velocity in Fig. 5. For the case of constant hook-load, however, increasing the angular velocity increases the corresponding axial velocity instead, while the average depth of cut remains roughly constant, see Fig. 6. We also note that the constant hook-load BC (28) seems to lead to more violent (higher amplitude) axial vibrations, see again Fig. 6 cf. Fig. 5.

The significance of $D(\bar{t})$ and $\beta(g(\bar{t}) - 1)$, as shown in Figs. 5 and 6, comes from (23). These quantities indicate the cutting and wearflat contributions, respectively, to the torque on bit. It holds that $g(\bar{t}) = 1$ at steady-state, such that $\beta(g(\bar{t}) - 1)$ correspond to changes in the wear-flat component. The total perturbed torque on bit equals the difference between these two plotted lines of $D(\bar{t})$ and $\beta(g(\bar{t}) - 1)$. The effect of the relative contributions of these components to the torque on bit will be investigated in the next section.

5.3. Evaluating the apparent velocity weakening effect

We aim to investigate the existence of the *apparent velocity-weakening effect* in the torque on bit. That is, to characterize the relation between the angular velocity of the bit (RPM) and the torque on bit. The term 'apparent velocity-weakening' is used in the literature to describe the effect that torque decreases for higher RPMs even though a rate-independent bit-rock interaction law is used [2,6,9,11,20]. Understanding this phenomenon is central to predicting and mitigating stick-slip oscillations. Previous studies on lumped-parameter models [6,9,11] have assumed a separation of time scales between the axial and torsional dynamics, such that the angular bit velocity can be assumed constant over an axial *quasi-limit-cycle*. The torque on bit can then be averaged to evaluate the occurrence of the apparent velocity-weakening effect. Although the assumption of time-scale separation does not necessarily hold for the distributed model in all parametric regimes, we will use a similar approach as it still yields insight in how the torque on bit at changes with changing RPMs in an averaged sense.

5.3.1. Constant axial top drive velocity

Recall that the non-dimensional weight on bit with the $g(\cdot)$ non-linearity writes

$$W_b(\bar{t}) = \frac{K_a}{\bar{c}} D(\bar{t}) + W_f g(\bar{t}). \tag{60}$$

and the non-dimensional torque on bit as

$$T_b(\bar{t}) = D(\bar{t}) + \beta W_f g(\bar{t}). \tag{61}$$

Next, we note that averaged over an axial limit cycle, or when averaged over an extended amount of time, the ROP (i.e. at the bit) must equal the velocity of the top-drive: otherwise, the strain in the drill-string would increase without bound. Consequently, for the constant top-drive velocity (i.e. BC (7)), the averaged depth of cut $\overline{D}$ over a limit cycle with period t_p satisfies

$$\frac{1}{t_p}\int_0^{t_p} D(\bar{t})\mathrm{d}\bar{t} = \overline{D} = \frac{V_0}{\Omega_0}. \tag{62}$$

Consequently,

$$\frac{1}{t_p}\int_0^{t_p} T_b(\bar{t})\mathrm{d}\bar{t} = \frac{V_0}{\Omega_0} + \beta W_f \frac{1}{t_p}\int_0^{t_p} g(\bar{t})\mathrm{d}\bar{t}, \tag{63}$$

and for situations without axial stick, e.g., for stable axial dynamics, such that $g(\bar{t}) = 1$, we obtain the (locally valid) velocity weakening effect

$$T_b(\Omega_b) - \beta W_f \approx \frac{V_0}{\Omega_0}. \tag{64}$$

When the axial dynamics are unstable, however, the drilling system will typically tend to an axial limit-cycle activating the $g(\cdot)$ non-linearity and reducing the torque on bit, see Fig. 5. If, as was indicated in Fig. 5, higher RPM is associated with less severe axial limit cycles and less activation of the $g(\cdot)$ non-linearity, this should result in a velocity strengthening effect.

5.3.2. Constant hook-load

From the weight on bit relation (60) we can obtain the following expression for the $g(\cdot)$ non-linearity

$$W_f g(\bar{t}) = \begin{cases} W_b(\bar{t}) - \frac{K_a}{\bar{c}} D(\bar{t}), & \text{Unstable axial dynamics} \\ W_f, & \text{Stable axial dynamics} \end{cases} \tag{65}$$

Thus, for the case of stable axial dynamics we obtain with averaging

$$\frac{1}{t_p}\int_0^{t_p} T_b(\bar{t})\mathrm{d}\bar{t} = \frac{1}{t_p}\int_0^{t_p} \frac{W_b(\bar{t})}{\frac{K_a}{\bar{c}}}\mathrm{d}\bar{t} \tag{66}$$

while in the general case

$$T_b(\bar{t}) = D(\bar{t}) + W_f \beta g(\bar{t}) \tag{67}$$

$$= D(\bar{t}) + \beta\left(W_b(\bar{t}) - \frac{K_a}{\bar{c}} D(\bar{t})\right) \tag{68}$$

$$= D(\bar{t})\left(1 - \beta\frac{K_a}{\bar{c}}\right) + \beta W_b(\bar{t}). \tag{69}$$

Averaging over a period t_p, and noting from (36) that at steady-state (and when averaged over time) $W_b \approx W_0$, we obtain

$$\frac{1}{t_p}\int_0^{t_p} T_b(\bar{t})\mathrm{d}\bar{t} = \frac{1}{t_p}\int_0^{t_p} \frac{V_b}{\Omega_b}\mathrm{d}\bar{t}\left(1 - \beta\frac{K_a}{\bar{c}}\right) + \beta W_0, \tag{70}$$

which indicates that, for the averaged case, the axial instability can contribute to a velocity weakening *or* a velocity strengthening effect depending on whether $\beta\frac{K_a}{\bar{c}} > 1$ or $\beta\frac{K_a}{\bar{c}} < 1$. Having said this, we should be careful to make sweeping conclusions based on such a simplified time-averaged analysis.

5.3.3. Averaging simulation study

To further analyze the averaged quantities, we consider the averaged "steady-state" wearflat and cutting contributions to the torque on bit over a range of imposed angular bit velocities. This is shown in Fig. 8 for constant axial top-drive velocity, BC (27), and Fig. 9 for constant hook-load, BC (28). Given the stability boundary

$$K_a M_{G,a} = 1, \tag{71}$$

since K_a is a scaling of the axial term of the characteristic equation, $G_a(s)$, plotting the normalized inverse gain margin, $M_{G,a}$, parametrized in Ω_b and η_a gives a complete parametrization of the stability of the axial loop. This is shown in Fig. 7, where the location of the set of parameters used in Figs. 8 and 9 is also indicated.

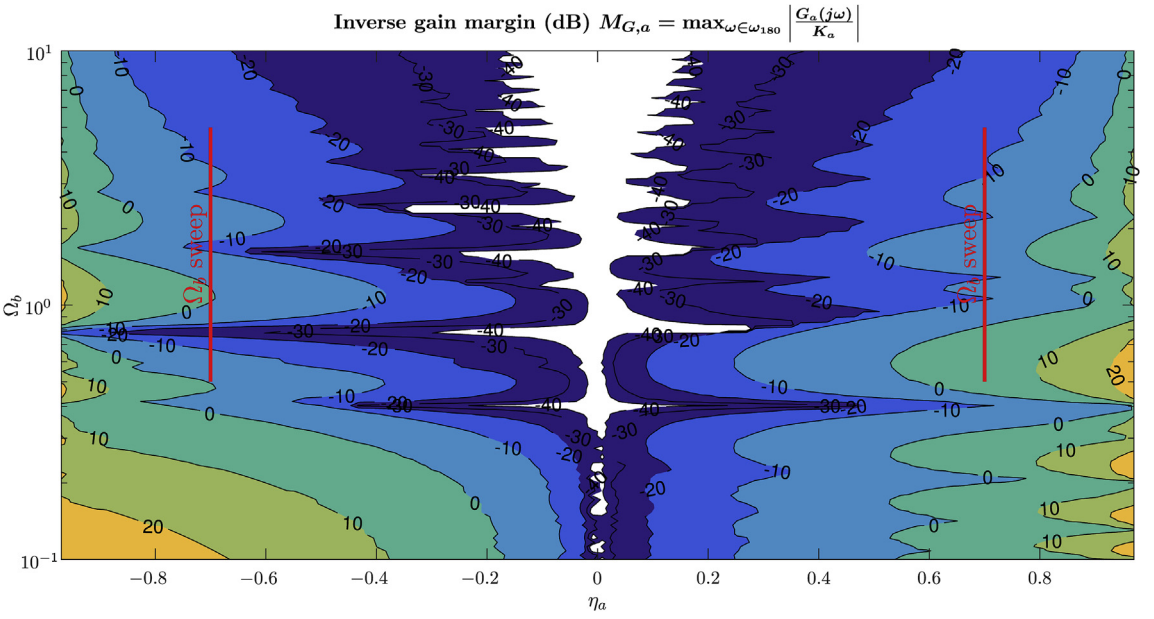

Fig. 7. Stability map of the axial uncoupled dynamics of the drill-string, following [5]. The map shows the inverse gain margin (in decibel), given as $M_{G,a} = \max_{\omega \in \omega_{180}} \left| \frac{G_a(j\omega)}{K_a} \right|$, such that instability occurs when $K_a > M_{G,a}$, see Ref. [5] for details. The line of Ω_b simulated in Figs. 8 and 9 are indicated by the red lines at $\eta_a = 0.7$ and $\eta_a = -0.7$, respectively. (For interpretation of the references to colour in this figure legend, the reader is referred to the Web version of this article.)

From Fig. 8, we note that higher K_a increases the impact of the wearflat forces (i.e. the $g(\cdot)$ nonlinearity) on the torque. This contribution to the torque on bit is further scaled with the β coefficient, which is set to $\beta = 0.1$ for this simulation study. Increasing β will increase the impact of the $g(\cdot)$ nonlinearity on the torque on bit. Given this fact, no monotonous velocity weakening or strengthening effect emerges from the wearflat force, but rather a potential alternating weakening and strengthening effect (depending on the magnitude of β), which seems to be related to the severity of the axial instabilities as indicated by Fig. 7.

Similarly, the averaged "steady-state" wearflat and cutting contributions to the total torque on bit over a range of imposed angular bit velocities, for the case of constant hook-load is shown in Fig. 9. Again, the location of this set of parameters in the stability map is indicated in Fig. 7. Also for this case we observe the alternating velocity strengthening and weakening effect of the averaged wearflat torque. For the angular velocity around $\Omega_b = 0.8$ the wearflat torque and force contribution is constant as the axial dynamics are stable at this RPM. This is consistent with the prediction of the stability map in Fig. 7. We note the change that happens in the torque on bit between $K_a = 10$ and $K_a = 20$. For $K_a = 10$ we have $\beta K_a / c_a = 0.625 < 1$, meaning that the axial instability (and activation of the $g(\cdot)$ nonlinearity) contributes with an increase in torque, while for $K_a = 20, 40$ the contribution is to that of a decrease in torque. This is consistent with the prediction from (70).

From the simulation study of the decoupled axial dynamics, we draw the following main conclusions:

- There is no uniform velocity weakening effect.
- The β parameter has an important qualitative effect on the torque on bit when the axial dynamics are unstable, as it relates the changes in the wearflat force W_f to changes in torque on bit.
- For constant topside axial velocity BC (7), Fig. 8, there can be both angular velocities where the torque on bit is velocity weakening and angular velocities where the torque is velocity strengthening. The velocity weakening effect seen is most prominent at lower velocities, and is predominantly associated with the cutting torque.
- For constant hook-load BC (8), Fig. 9, the averaged velocity weakening effect due to the cutting is less prominent. However, ROP increases with increased bit velocity Ω_b and when the axial dynamics are unstable.
- The axial instability can be related to different resonance modes of the drill-string dynamics, which is a property that cannot be replicated with a lumped-parameter model capturing a single axial mode. Typically, several axial modes are unstable, and sometimes the first (low-frequency) mode, captured by lumped-parameter models, is stable, while higher frequency modes are unstable. In this case the lumped-parameter model would erroneously predict stability.

6. Global dynamic analysis of the coupled axial-torsional dynamics

In this section, we perform a simulation study of the full coupled model given in Section 3.2.

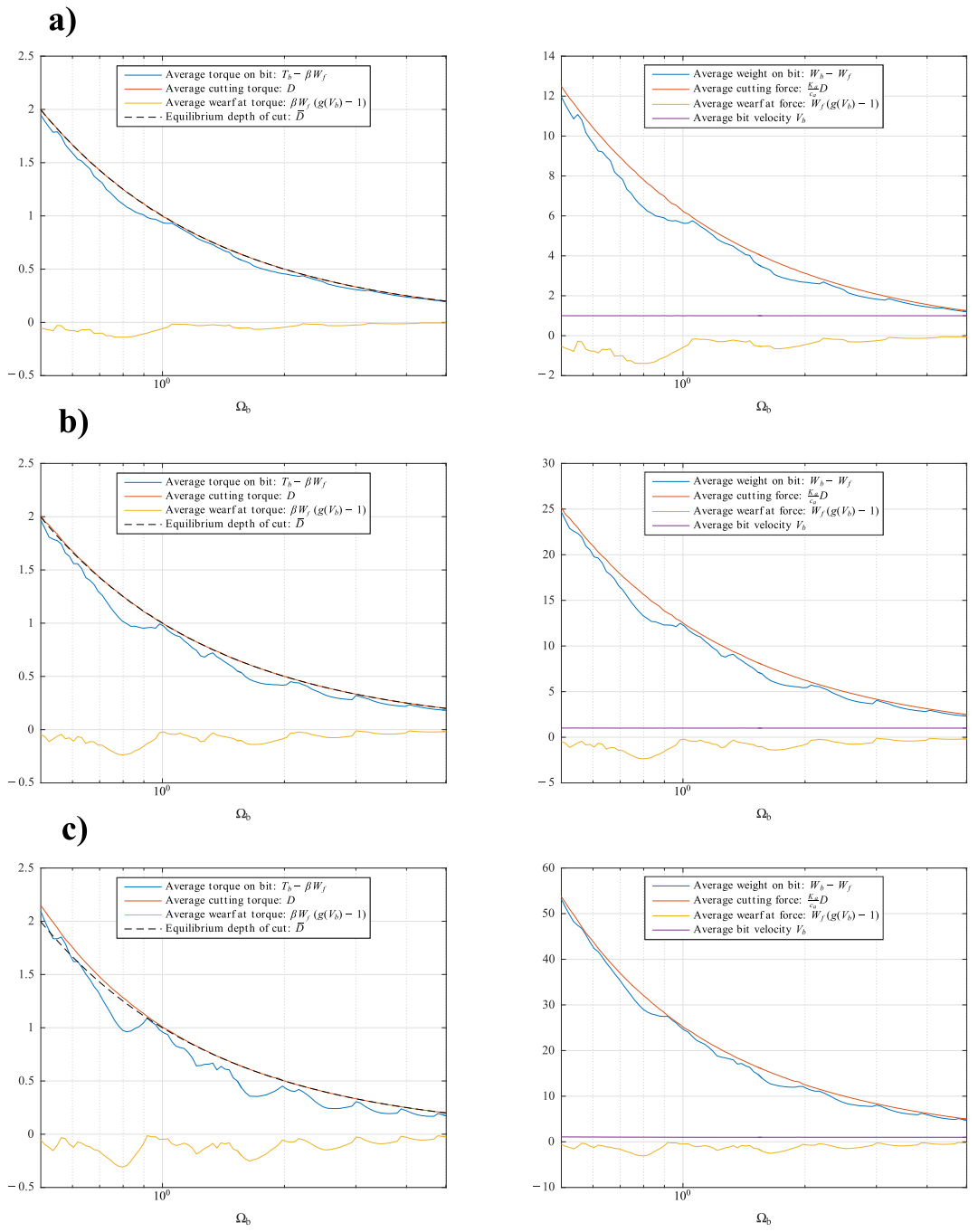

Fig. 8. The averaged torque (left) and forces (right) on bit resulting from simulating the uncoupled axial dynamics at a constant angular bit velocity Ω_b, parametrized in the angular bit velocity Ω_b, with $\beta = 0.1$. The positive $\eta_a = 0.7$ corresponds to the imposed axial velocity topside boundary condition (27) with $V_0 = 1$. Axial gains are **a)** $K_a = 10$, **b)** $K_a = 20$, **c)** $K_a = 40$.

6.1. Characteristic quantities of the coupled system

The relative torsional wave velocity compared to the axial wave velocity is given by the square root of the relative magnitude of the shear and Young's modulus of the drill-string, i.e., for typical values of E and G

$$t_a^* = \sqrt{\frac{E}{G}}\, t^* \approx \sqrt{\frac{79\ \text{GPa}}{200\ \text{GPa}}}\, t^* \approx \frac{1}{1.6} t^*, \tag{72}$$

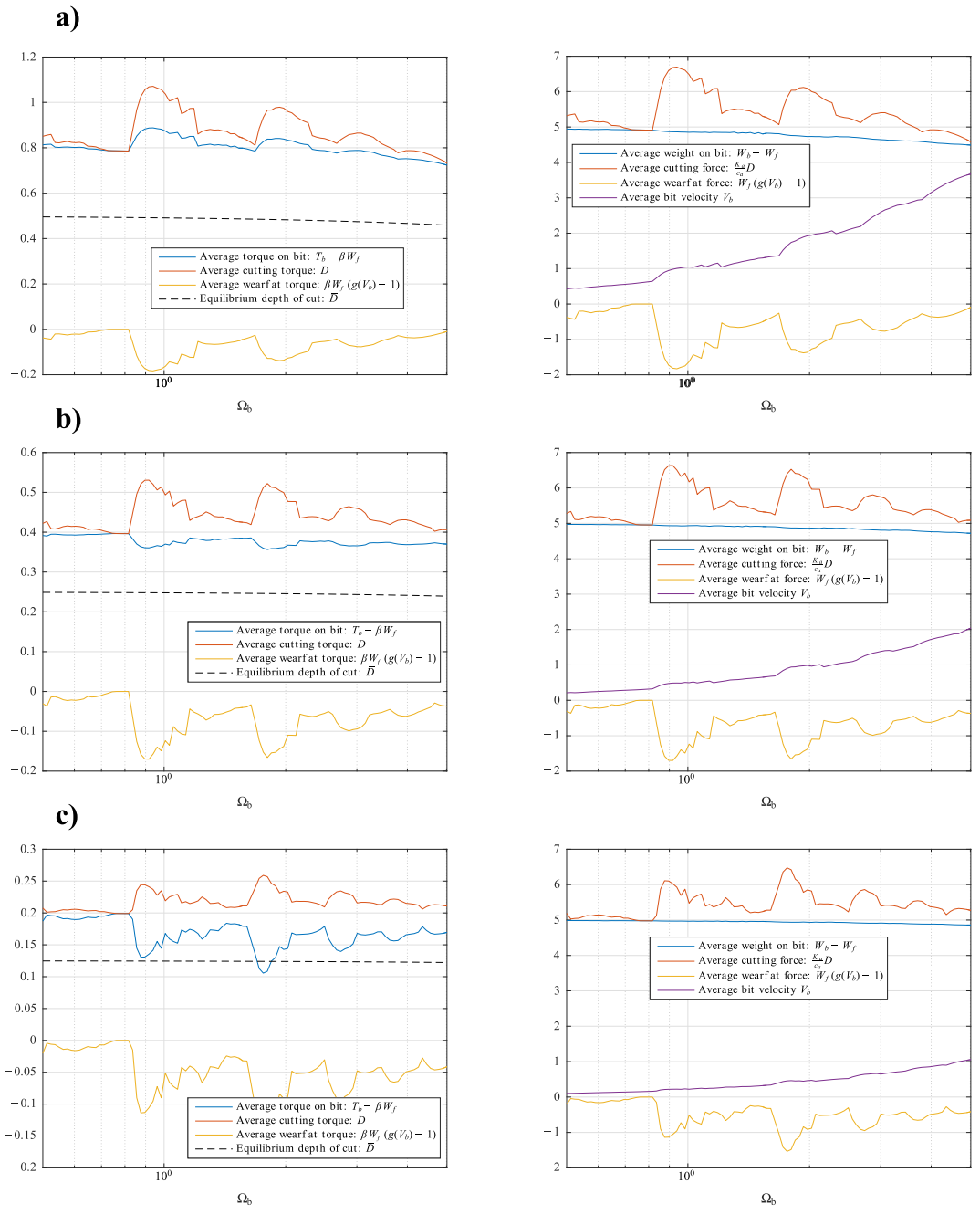

Fig. 9. The averaged torque (left) and forces (right) on bit resulting from simulating the uncoupled axial dynamics at a constant angular bit velocity Ω_b, parametrized in the angular bit velocity Ω_b, with $\beta = 0.1$. The negative $\eta_a = -0.7$ corresponds to the hook-load topside boundary condition (28) with $W_0 - W_f = 5$. Axial gains are **a)** $K_a = 10$, **b)** $K_a = 20$, **c)** $K_a = 40$.

equating to

$$\overline{c} = 1.6, \tag{73}$$

and we will assume this as constant to limit the number of free parameters in the study below.

As the axial drill-string characteristic time is assumed fixed relative to the torsional time and the torsional time is used to non-dimensionalize the independent variable of time, there are four remaining characteristic quantities for the torsional and axial feedback loops:

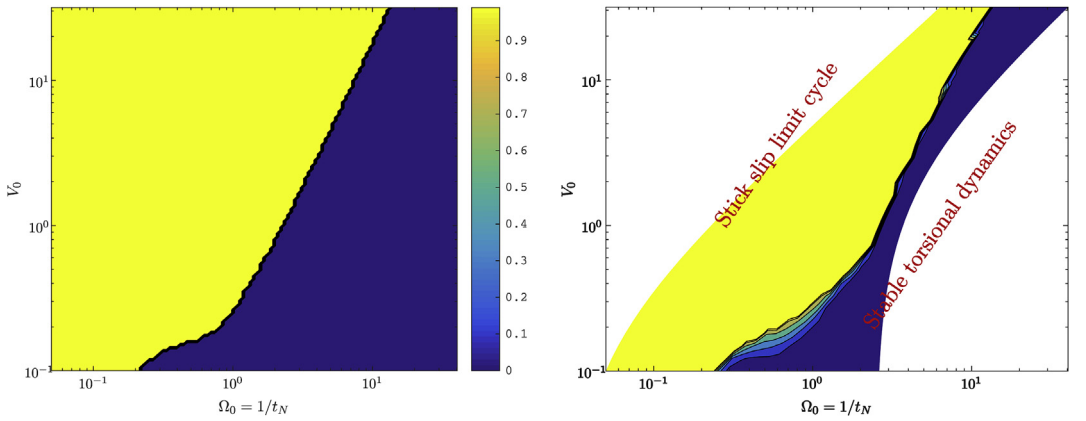

Fig. 10. Stability maps of the torsional uncoupled dynamics of the drill-string (i.e. $K_a = 0$), derived in the frequency domain (left) using the Nyquist criterion [7] where yellow indicates torsional instability and dark blue indicates stability. The equivalent stability map by evaluating simulations (right), where yellow indicates $M_T = 1$ and dark blue indicates $M_T < 0.1$, see (75). (For interpretation of the references to colour in this figure legend, the reader is referred to the Web version of this article.)

- Nominal axial velocity V_0 or W_0, for BC (27) and (28), respectively,
- Axial loop gain K_a,
- Pseudo reflection coefficients η_a, η_t.

Additionally, there are two characteristic quantities arising from the bit-rock interaction

- Angular top-drive velocity Ω_0, which determines the nominal delay of the bit-rock interaction t_N, through the relation: $t_N = \frac{1}{\Omega_0}$.
- β appearing in the torsional bit-rock interaction law, giving the effect of the $g(\cdot)$ non-linearity on torque on bit, see (64).

Throughout this section, we fix the following parameters:

- $\beta = 0.1$
- $\eta_t = 0.7$.
- $\eta_a = \pm 0.7$ for BC (27) and (28), respectively.

The three remaining characteristic quantities: Ω_0, K_a, and V_0 or W_0, are considered within representative ranges.

6.2. Torsional stability, sticks slip occurrence

In the absence of the coupling to the axial dynamics, i.e. for $K_a = 0$, the stability of the torsional dynamics is determined by the torsional part of the characteristic equation

$$G_t(s) = -g_t(s)\frac{1}{s}\frac{\overline{V}}{\overline{\Omega}}\left(1 - \mathrm{e}^{-s/\Omega_0}\right). \tag{74}$$

We aim to gage the occurrence of stick-slip oscillations, and parametrize this occurrence in the key parameters of the system. Towards this end, we perform simulations with the full coupled non-linear model initialized at the equilibrium and then subject to a 15 second square wave added to the weight on bit to perturb the system away from the equilibrium. The simulation is run for 120 dimensionless time units, and then the existence and magnitude of the torsional limit cycles are evaluated by introducing the following metric

$$M_T = \frac{\Omega_0 - \min_t \Omega_b(\bar{t})}{\Omega_0}, \tag{75}$$

where $M_T = 1$ indicates a limit cycle that involves torsional stick, i.e., a *stick-slip* limit cycle and $M_T = 0$ indicates a stable steady-state (constant torsional velocity) solution.

6.2.1. Constant top-drive velocity

We initially study the case of constant imposed top-drive velocity, i.e., using the BC (27). We consider the case of $K_a = 0$, which implies that the linear torsional dynamics are uncoupled from the axial ones. This also means that the characteristic

equation reduces to the torsional term, i.e.,

$$G(s) = G_t(s). \tag{76}$$

The corresponding stability map, for $\eta_t = 0.70$ (i.e. BC (7)) and parametrized in imposed topside velocity V_0, is shown in Fig. 10. We expect the non-local torsional dynamics to be dominated by the (non)-occurrence of the torsional instability. This expectation is confirmed in simulations, the result of which is illustrated in Fig. 10 which compares the result of the Nyquist criteria evaluated in the frequency domain and the result of simulating the non-linear dynamics. The occurrence of stick-slip limit cycles closely matches the existence of an unstable pole, as indicated by the Nyquist stability criterion by $M_G > 0$ dB, for the case of $K_a = 0$. This is a significant validation of the numerical implementation of the distributed, non-linear model, as it indicates that the behavior is consistent with the stability results of [5,7].

Having established the coherence between the previous analytical stability results and the behavior of our simulation model, and, furthermore, established a baseline for behavior of the uncoupled torsional dynamics, we now introduce the axial coupling by setting $K_a > 0$ and evaluate the effect on the M_T metric of (75). The effect that the axial loop gain $K_a > 0$ has on the occurrence of stick-slip limit cycles is illustrated in Fig. 11. The main conclusion from this figure is that increasing the axial loop gain has a stabilizing effect on the torsional dynamics. Furthermore, while some of the qualitative properties of the shape of the unstable region are conserved (generally, increasing V_0 has a *destabilizing* effect while increasing Ω_0 has a *stabilizing* effect), the local result alone is clearly insufficient to evaluate the occurrence of stick-slip oscillations: the greater K_a, the more dissimilar are the local and the nonlocal stability maps. This is related to our final takeaway from this figure: the interaction between the

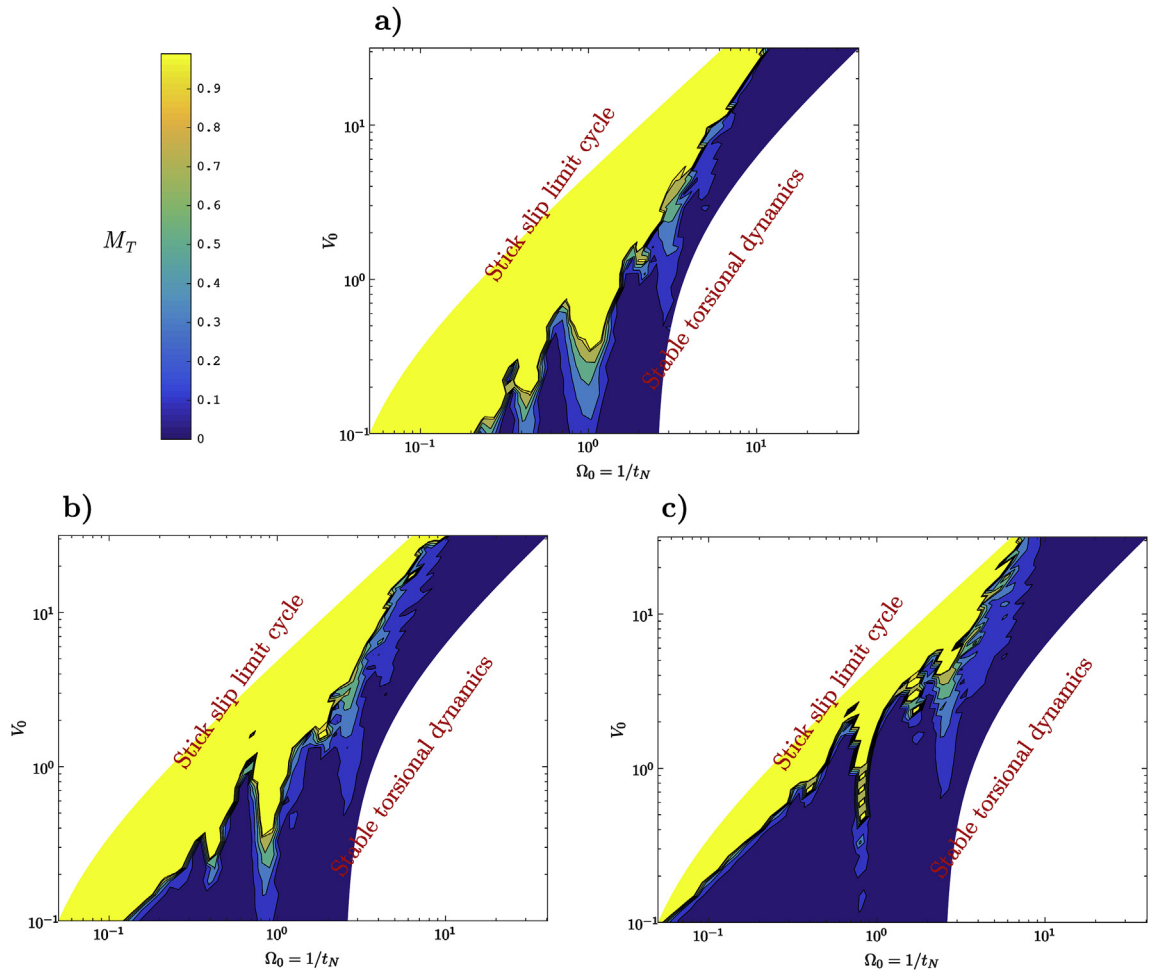

Fig. 11. The three plots above shows the effect of the axial loop gain, K_a, on the stability of the torsional dynamics, specifically for **a)** $K_a = 10$, **b)** $K_a = 20$, **c)** $K_a = 40$. Yellow indicates $M_T = 1$, as given in (75), meaning a *stick-slip* limit cycle, and dark blue indicates $M_T < 0.1$ meaning stable torsional dynamics. Somewhat surprisingly, increasing K_a, and hence making the axial instability more severe, tends to have a stabilizing effect on the torsional dynamics. The more complicated map, compared to the decoupled one in Fig. 10 is due to the interaction between the axial and torsional limit cycles. (For interpretation of the references to colour in this figure legend, the reader is referred to the Web version of this article.)

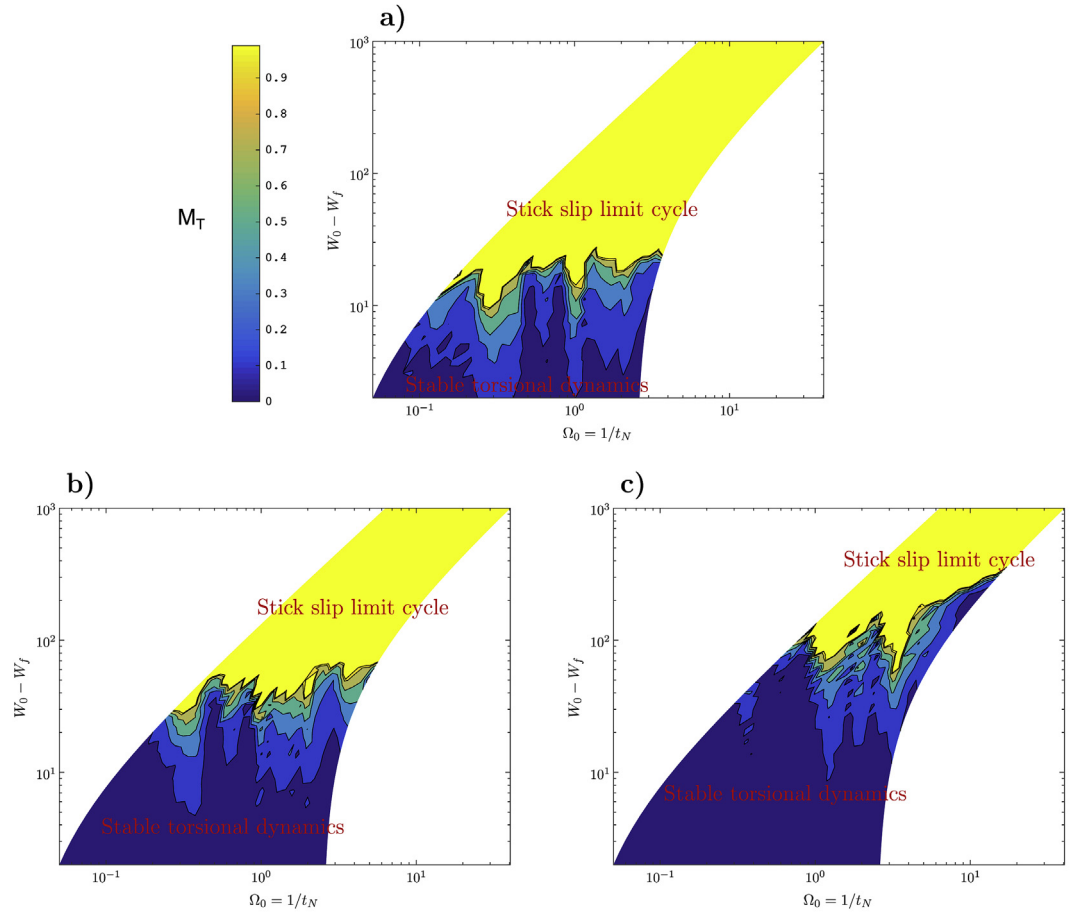

Fig. 12. The four plots give the occurrence of torsional stick-slip parametrized in angular velocity, Ω_0, and hook-load W_0, i.e., for the case of using BC (28), with $\beta = 0.1$ and for axial loop gain **a)** $K_a = 10$, **b)** $K_a = 20$, **c)** $K_a = 40$. Yellow indicates $M_T = 1$, as given in (75), meaning a *stick-slip* limit cycle, and dark blue indicates $M_T < 0.1$ meaning stable torsional dynamics. (For interpretation of the references to colour in this figure legend, the reader is referred to the Web version of this article.)

axial non-linear dynamics and the torsional ones results in a significantly more complex topology of the stability map than what is seen in the linear case, the uncoupled case or in the lumped parameter case. In particular, we note the appearance of *peninsulas* of 'stick-slip limit cycles' along certain RPMs (Ω_0), see Fig. 11. These peninsulas seem to roughly remain along the same RPMs for changing K_a, and indicate the counter-intuitive results that in specific cases reducing the RPM will remove a stick-slip limit cycle.

6.2.2. Constant hook-load

Next, we consider the case of constant imposed hook-load, i.e., using BC (28). For this case, the equilibrium velocity will be dependent on the axial loop gain K_a, as indicated by (38). Furthermore, the average axial velocity depends on the nature of the axial limit cycle, and is not necessarily equivalent to the equilibrium axial velocity $\overline{V}$. The results for different K_a is shown in Fig. 12.

To understand these stability maps, recall the torsional characteristic equation

$$G_t(s) = -g_t(s)\frac{1}{s}\frac{\overline{V}}{\overline{\Omega}}\left(1 - \mathrm{e}^{-s/\Omega_0}\right), \tag{77}$$

where the torsional nominal loop gain, given by $K_t = \frac{\overline{V}}{\overline{\Omega}}$, is key for stability. Inserting the expression for equilibrium ROP $\overline{V}$, (38), we have

$$K_t = \frac{\overline{c}}{K_a}\left(W_b - W_f\right) = \frac{1}{\frac{\overline{k}_a}{\overline{c}^2}\Omega_0 + \frac{K_a}{\overline{c}}}\left(W_0 - W_f\right) \tag{78}$$

$$\approx \frac{\overline{c}}{K_a}\left(W_0 - W_f\right), \tag{79}$$

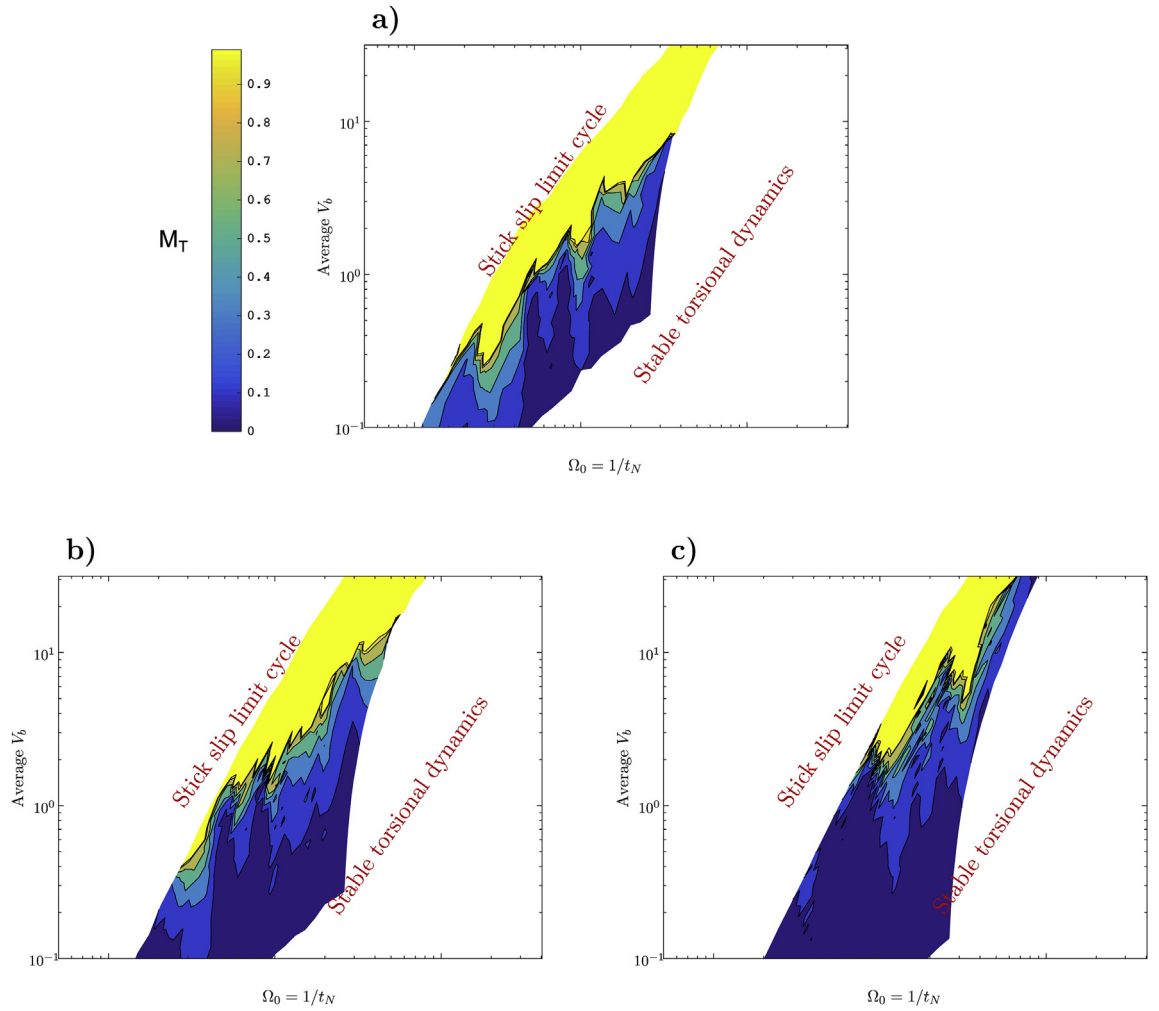

Fig. 13. The four plots give the occurrence of torsional stick-slip parametrized in angular velocity, Ω_0, and calculated ROP averaged over 30 time units: $\frac{1}{30}\int_{30}^{60} V_b(\bar{t})\mathrm{d}\bar{t}$, for the case of using BC (28) (i.e., equivalent to Fig. 12), with $\beta = 0.1$ and axial loop gain **a)** $K_a = 10$, **b)** $K_a = 20$, **c)** $K_a = 40$. Yellow indicates $M_T = 1$, as given in (75), meaning a *stick-slip* limit cycle, and dark blue indicates $M_T < 0.1$ meaning stable torsional dynamics. (For interpretation of the references to colour in this figure legend, the reader is referred to the Web version of this article.)

where the last approximation comes from noting that typically $\bar{k}_a \ll K_a$. That means that the nominal torsional loop gain might be considered approximately independent of the top drive velocity, Ω_0, while inversely proportional to the axial loop gain K_a, and increasing with weight on bit $W_b - W_f$. Of course, these conclusions from (79), are only valid close to the equilibrium and will not necessarily hold in a nonlocal sense if the axial dynamics are unstable.

Studying Fig. 12, we note that stability boundary roughly follows a horizontal line along a specific value of weight on bit $W_0 - W_f$. Furthermore, comparing the cases $K_a = 10, 20, 40$, given in **a)**, **b)** and **c)**, respectively, we find that this line approximately lies at the values $W_0 - W_f = 10, 20, 40$, and indeed changes with K_a. Given this simulation result, it is tempting to propose the rough heuristic that the stability boundary lies around

$$W_0 - W_f = K_a. \tag{80}$$

The latter boundary, in the physical parameters, equates to

$$w_0 - w_f = K_a w^* = \frac{\bar{c}\zeta JG2\pi}{aNL}. \tag{81}$$

Beyond this main observation, we again find the existence of peninsulas of instability around certain RPMs, the location of which seem to vary somewhat with K_a, and are expected to be due to the complex interaction between the axial and torsional instability.

To give a more direct comparison with the result of the constant topside axial velocity BC of Fig. 11, the result of Fig. 12 is also shown in Fig. 13 but here parametrized in the calculated averaged ROP$= \frac{1}{30}\int_{30}^{60} V_b(\bar{t})\mathrm{d}\bar{t}$. In this figure, we observe that the

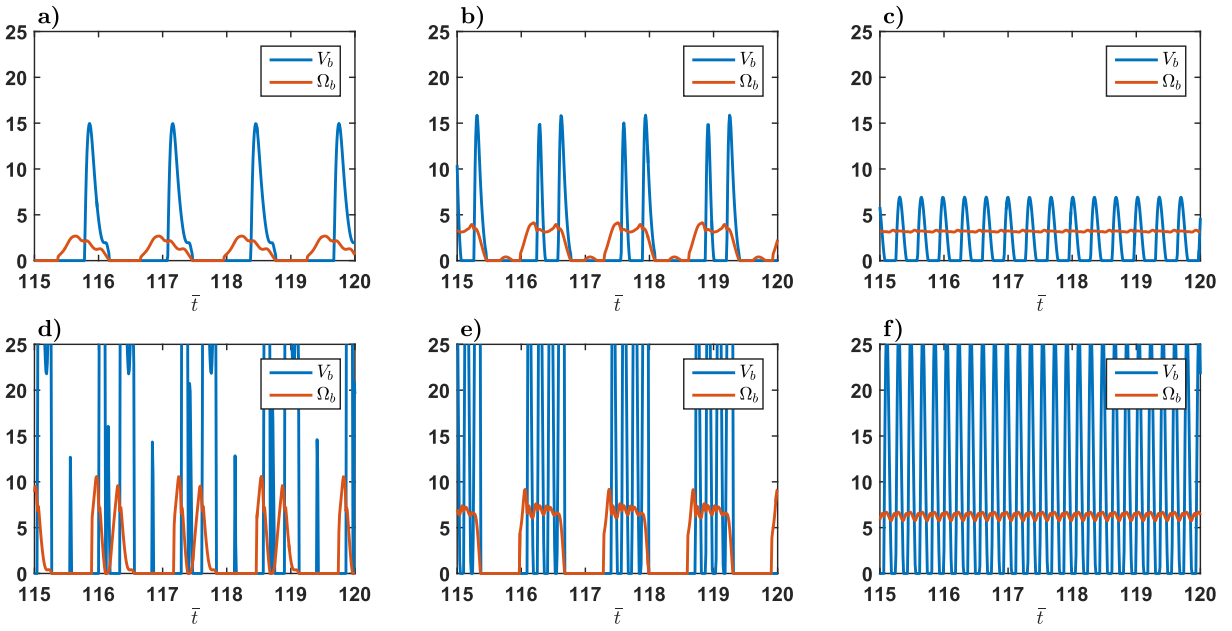

Fig. 14. Time-domain simulations of the coupled model, with $\eta_a = \eta_t = 0.7$ and **a)** $V_0 = 2.0, \Omega_0 = 1.0$, **b)** $V_0 = 2.0, \Omega_0 = 1.8$, **c)** $V_0 = 2.0, \Omega_0 = 3.2$. **d)** $V_0 = 10, \Omega_0 = 2.2$, **e)** $V_0 = 10, \Omega_0 = 3.5$, **f)** $V_0 = 10, \Omega_0 = 6.3$.

general shape of Fig. 11 is retained also for the constant hook-load BC: that is, the general trend concerning the boundary of stability goes along a diagonal between ROP and angular velocity, where increasing RPM (holding ROP constant) or decreasing ROP (holding RPM constant) leads to stability. Again we also see that increasing the axial loop gain K_a has a stabilizing effect.

6.3. Illustrative time-domain simulations

To illustrated some of the features of the developed non-local torsional stability maps of Fig. 11, we next consider the time series for a set of angular and axial velocities and with the axial loop gain $K_a = 20$. These time series are shown in Fig. 14,

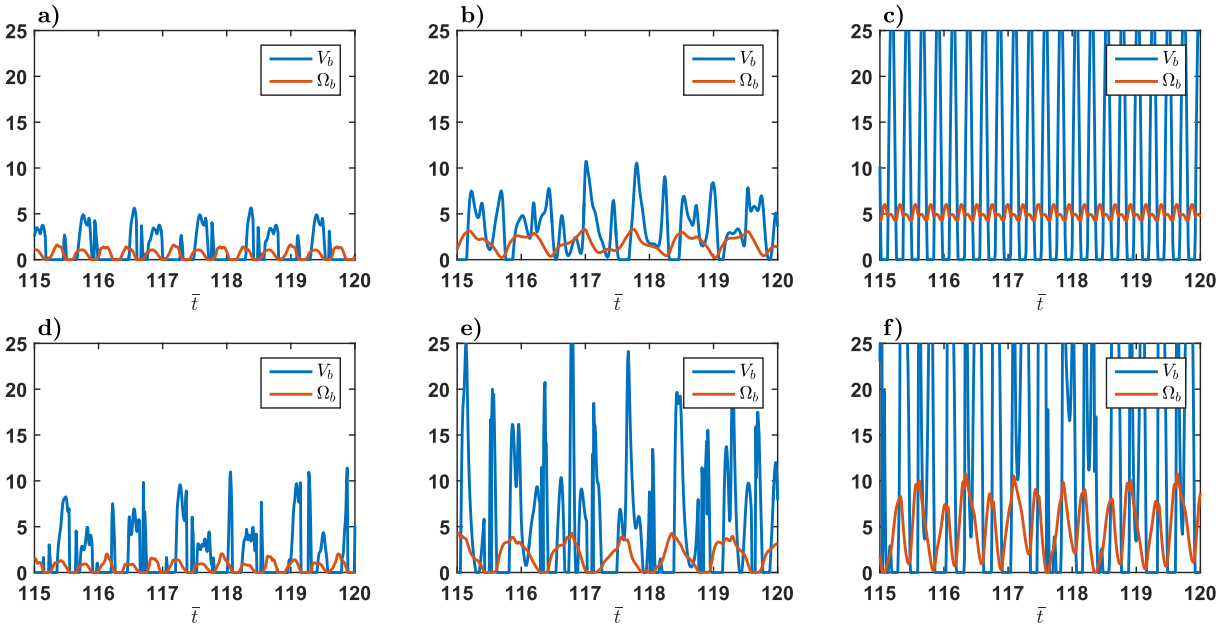

Fig. 15. Time-domain simulations of the coupled model, with $\eta_a = -0.7, \eta_t = 0.7$ (i.e. constant hook-load BC) and **a)** $W_0 - W_f = 40, \Omega_0 = 0.6$, **b)** $W_0 - W_f = 40, \Omega_0 = 1.8$, **c)** $W_0 - W_f = 40, \Omega_0 = 5.0$. **d)** $W_0 - W_f = 64, \Omega_0 = 0.6$, **e)** $W_0 - W_f = 64, \Omega_0 = 1.8$, **f)** $W_0 - W_f = 64, \Omega_0 = 5.0$.

corresponding to Fig. 11 **b)**, and Fig. 15, corresponding to Fig. 12 **b)**. This set of time series examples give an impression of the shape of the different limit-cycle dynamics that the system can exhibit. From these time-domain examples simulation results, we make the following observations:

- The time-domain examples qualitatively illustrates the overview provided by the stability maps in Figs. 11 and 12.
- For the low RPMs used in Fig. 14, there is no significant time-scale separation between the axial and torsional dynamics. For higher RPMs, however, one can argue for such a time-scale separation.
- Also from Fig. Fig. 14, note how increasing the RPM seems to increase the frequency of the axial, but not the torsional, oscillations.
- For constant hook load, see Fig. 15, increasing the RPM decreases the axial cutting force and results in higher amplitude axial vibrations.

7. Conclusions

In this paper, we have considered a distributed axial-torsional drill-string model with a rate-independent bit-rock interaction law to study the occurrence of axial and torsional self-excited vibrations as caused by the regenerative effect induced by the bit-rock interaction. The main conclusions from the paper are as follows:

- In Refs. [5,7] it was shown that, typically, multiple axial modes are simultaneously unstable. We find that, for severe axial instabilities, several of these unstable modes are represented also in the axial *quasi* limit-cycle with the full non-linear dynamics. A notable point is that sometimes the first (low-frequency) axial mode is stable, while higher frequency modes are unstable. In this case, the lumped-parameter model would erroneously predict stability. This makes analysis with a simplified lumped-parameter model less valid for these cases and a distributed description of the dynamics is indeed needed.
- The frequency of the axial limit-cycles are determined by the top drive RPM. This fact has been suggested by Refs. [5,7] and is confirmed in the simulation studies of the present paper. However, as is also shown in Refs. [5,7], the frequency of the torsional oscillations will in most cases coincide with the first torsional resonant frequency of the drill-string.
- The bit-rock interaction is nominally *velocity weakening* (as can be seen from the linearization), however, the effect of the $g(\cdot)$ non-linearity (induced by the wearflat-rock contact) tends to be *velocity strengthening*. The result of the combined effects is complex as it can exhibit alternating velocity weakening and strengthening effects at different RPMs.
- The type of top-side axial boundary condition, constant top-drive velocity vs. constant hook load, has a crucial effect on the stability of the torsional dynamics, and furthermore, changes the qualitative impact the characteristic quantities have on stability.

For constant axial top-drive velocity:

- The occurrence of torsional stick-slip roughly matches the stability predictions of the linearized torsional loop.
- Increasing the RPM, Ω_0, has a major stabilizing effect.
- Increasing the axial loop gain, thus the severity of the axial instability, has a stabilizing effect on the tendency to develop torsional stick-slip oscillations. A similar result was obtained with a lumped-parameter model in Ref. [21].

For constant axial hook-load:

- Increasing RPM has a less significant stabilizing effect.
- Increasing the nominal axial loop gain, will tend to reduced the steady-state ROP, thus reducing the torsional nominal loop gain, which has a stabilizing effect.
- Based on the simulation results, we proposed the stability heuristic that the stick-slip instability occurs when the non-dimensional weight on bit, subtracted the wearflat component, is greater than the axial loop gain.

Acknowledgment

This work was supported by the Research Council of Norway, ConocoPhillips, AkerBP, Statoil and Wintershall through the research center DrillWell (203525/O30) at IRIS, and through a MSCA Individual Fellowship by European Union's Seventh Frame-

work Programme for research, technological development and demonstration under Marie Curie grant agreement no [608695], through FRIPRO Mobility Grant Fellowship Programme (FRICON).

Appendix A. Derivation of the non-dimensional model formulation

We normalize all variables with characteristic quantities, denoted by the * superscript, to be decided:

$$\bar{t} = \frac{t}{t^*} \tag{A.1}$$

$$\bar{x} = \frac{x}{x^*} \tag{A.2}$$

$$V = \frac{v}{v^*} \tag{A.3}$$

$$W = \frac{w}{w^*} \tag{A.4}$$

$$\Omega = \frac{\omega}{\omega^*} \tag{A.5}$$

$$T = \frac{\tau}{\tau^*} \tag{A.6}$$

$$\Lambda = \frac{\lambda}{d^*}. \tag{A.7}$$

The problem is now to decide on appropriate characteristic quantities in (A.1)–(A.7). As the independent variable of position lives in the domain $x \in [0, L]$, we use the drill-string length to normalize it, i.e. $x^* = L$. This yields, based on (3), (4), (A.1)–(A.7), the following torsional wave equation:

$$\frac{\partial T(\bar{t},\bar{x})}{\partial \bar{t}}\frac{\tau^*}{t^*} + JG\frac{\partial \Omega(\bar{t},\bar{x})}{\partial \bar{x}}\frac{\omega^*}{L} = 0 \tag{A.8}$$

$$J\rho\frac{\partial \Omega(\bar{t},\bar{x})}{\partial \bar{t}}\frac{\omega^*}{t^*} + \frac{\partial T(\bar{t},\bar{x})}{\partial \bar{x}}\frac{\tau^*}{L} = -k_t\rho J\omega^*\Omega(\bar{t},\bar{x}). \tag{A.9}$$

We collect the coefficients in (A.8), (A.9) to obtain

$$\frac{\partial T(\bar{t},\bar{x})}{\partial \bar{t}} + \frac{\partial \Omega(\bar{t},\bar{x})}{\partial \bar{x}}JG\frac{\omega^*}{L}\frac{t^*}{\tau^*} = 0 \tag{A.10}$$

$$\frac{\partial \Omega(\bar{t},\bar{x})}{\partial \bar{t}} + \frac{\partial T(\bar{t},\bar{x})}{\partial \bar{x}}\frac{1}{J\rho}\frac{\tau^*}{L}\frac{t^*}{\omega^*} = -k_t t^*\Omega(\bar{t},\bar{x}). \tag{A.11}$$

Now, define the characteristic torque

$$\tau^* = \frac{JG\omega^* t^*}{L}, \tag{A.12}$$

with which (A.10), (A.11) reduces to

$$\frac{\partial T(\bar{t},\bar{x})}{\partial \bar{t}} + \frac{\partial \Omega(\bar{t},\bar{x})}{\partial \bar{x}} = 0 \tag{A.13}$$

$$\frac{\partial \Omega(\bar{t},\bar{x})}{\partial \bar{t}} + \frac{\partial T(\bar{t},\bar{x})}{\partial \bar{x}}\frac{Gt^{*2}}{\rho L^2} = -k_t t^*\Omega(\bar{t},\bar{x}). \tag{A.14}$$

Given the above, we choose

$$t^* = L\sqrt{\frac{\rho}{G}} = \frac{L}{c_t} := t_t, \tag{A.15}$$

which is the torsional wave travel time. (A.15) yields (29)–(30).

Similarly, for the axial wave equation, (1)–(2), we obtain

$$\frac{\partial W(\bar{t},\bar{x})}{\partial \bar{t}} + \frac{\partial V(\bar{t},\bar{x})}{\partial \bar{x}}\frac{v^*}{L}\frac{t_t}{w^*}AE = 0 \tag{A.16}$$

$$\frac{\partial V(\bar{t},\bar{x})}{\partial \bar{t}} + \frac{\partial W(\bar{t},\bar{x})}{\partial \bar{x}}\frac{w^*}{L}\frac{t_t}{v^*}\frac{1}{A\rho} = -k_a t_t V(\bar{t},\bar{x}). \tag{A.17}$$

Hence, choosing $w^* = \frac{AEv^*t_t}{L}$ in (A.16), (A.17), gives

$$\frac{\partial W(\bar{t},\bar{x})}{\partial \bar{t}} + \frac{\partial V(\bar{t},\bar{x})}{\partial \bar{x}} = 0 \tag{A.18}$$

$$\frac{\partial V(\bar{t},\bar{x})}{\partial \bar{t}} + \frac{\partial W(\bar{t},\bar{x})}{\partial \bar{x}} \frac{t_t^2}{t_a^2} = -k_a t_t V(\bar{t},\bar{x}), \tag{A.19}$$

where $\frac{t_t^2}{t_a^2} = \frac{c_a^2}{c_t^2} := \bar{c}^2$, and $c_a = \sqrt{E/\rho}, c_a = \sqrt{G/\rho}$ is the axial and torsional, respectively, sound velocity of the drill-string.

Finally, we consider the bit rock interaction transport equation (9), using (A.7):

$$\frac{\partial \Lambda(t,\theta)}{\partial \bar{t}} \frac{d^*}{t_t} + \Omega_b(\bar{t})\omega^* \frac{N}{2\pi} \frac{\partial \Lambda(\bar{t},\theta)}{\partial \theta} d^* = v^* V_b(\bar{t}), \tag{A.20}$$

and collecting coefficients

$$\frac{\partial \Lambda(t,\theta)}{\partial \bar{t}} + \Omega_b(\bar{t}) \frac{\partial \Lambda(\bar{t},\theta)}{\partial \theta} \omega^* t_t \frac{N}{2\pi} = \frac{v^* t_t}{d^*} V_b(\bar{t}), \tag{A.21}$$

we find

$$\omega^* = \frac{2\pi}{t_t N}, \qquad v^* = \frac{d^*}{t_t}. \tag{A.22}$$

We choose to set the remaining scaling parameter, d^*, such that

$$T_b(\bar{t}) = a^2 \epsilon N \frac{d^*}{\tau^*} D(t) + \beta W_f = D(t) + \beta W_f, \tag{A.23}$$

i.e. $d^* = \frac{\tau^*}{a^2 \epsilon N}$.

Appendix B. Interpretation of characteristic quantities

- $t^* = t_t = L/c_t$ is the travel time of the torsional drill-string wave.
- $x^* = L$ is the length of the drill-string.
- $v^* = d^*/t_t = \frac{1}{a^2 \epsilon N} \frac{JG}{L} \frac{2\pi}{N t_t}$ is the velocity corresponding to the length of the characteristic depth of cut per drill-string wave travel time.
- $w^* = \frac{AEv^*}{c_a} \bar{c} = \frac{AE}{L} d^*$ is the (scaled by $\bar{c}$) characteristic impedance of the drill-string multiplied with the characteristic axial velocity v^*. It is also the axial force required to displace the bit by the length corresponding to the characteristic depth of cut d^*.
- $\omega^* = \frac{2\pi}{t_t N}$ is the angle between two cutters, $2\pi/N$, over the drill-string travel time t_t, i.e. $\Omega_0 = 1$ entails that the steady-state delay between two cutters equals the drill-string travel time.
- $\tau^* = \frac{JG\omega^* t^*}{L} = \frac{JG}{L} \frac{2\pi}{N}$ is the torque required to rotate a semi-infinite drill-string with the characteristic angular velocity ω^*, which can be seen by noting that $\frac{JGt^*}{L}$ is the torsional impedance of the drill-string, cf. [5]. It also corresponds to the torque required to angularly displace the drill-string the angular distance between two blades.
- $d^* = \frac{\tau^*}{a^2 \epsilon N} = \frac{1}{a^2 \epsilon N} \frac{JG}{L} \frac{2\pi}{N}$ is the length corresponding to a depth of cut that create the characteristic torque τ^*.

Appendix C. Derivation of drill string transfer functions

The drill string transfer functions used in this paper have been derived in Ref. [5] and are included here for completeness. The following derivation uses the transmission line model formulation known as the transfer matrix approach [22–24].

The characteristic line impedances $Z_i, i \in \{a,t\}$, and propagation operators, $\Gamma_i, i \in \{a,t\}$, for (24)–(25) and (29)–(30), respectively, are given as

$$Z_a(s) = \left(1 + \frac{\bar{k}_a}{s}\right)^{1/2}, \qquad \Gamma_a(s) = \frac{s}{\bar{c}} \left(1 + \frac{\bar{k}_a}{s}\right)^{1/2}, \tag{C.1}$$

$$Z_t(s) = \left(1 + \frac{\bar{k}_t}{s}\right)^{1/2}, \qquad \Gamma_t(s) = s \left(1 + \frac{\bar{k}_t}{s}\right)^{1/2}, \tag{C.2}$$

Now the axial and torsional distributed systems both satisfy the well-known closed-form general solution of transmission lines which can be given as a two-port configuration [25,26]:

$$\begin{bmatrix} W_b(s) \\ V_b(s) \end{bmatrix} = \begin{bmatrix} \cosh\Gamma_a & -Z_a \sinh\Gamma_a \\ -\frac{1}{Z_a}\sinh\Gamma_a & \cosh\Gamma_a \end{bmatrix} \begin{bmatrix} W_0(s) \\ V_0(s) \end{bmatrix}, \quad \begin{bmatrix} T_b(s) \\ \Omega_b(s) \end{bmatrix} = \begin{bmatrix} \cosh\Gamma_t & -Z_t \sinh\Gamma_t \\ -\frac{1}{Z_t}\sinh\Gamma_t & \cosh\Gamma_t \end{bmatrix} \begin{bmatrix} T_0(s) \\ \Omega_0(s) \end{bmatrix}, \tag{C.3}$$

At the topside boundary, i.e. at $x = 0$, we have $\widetilde{\Omega}_0 = 0$ and either $\widetilde{W}_0 = 0$ for BC (28), or $\tilde{V}_0 = 0$ for (27). Combining this with (C.3) we obtain the relations (39), (40).

References

[1] S. Jardine, D. Malone, M. Sheppard, Putting a damper on drilling's bad vibrations, Oilfield Rev. 1 (January) (1994) 15–20.
[2] C. Germay, V. Denoël, E. Detournay, Multiple mode analysis of the self-excited vibrations of rotary drilling systems, J. Sound Vib. 325 (aug 2009) 362–381.
[3] A. Depouhon, E. Detournay, Instability regimes and self-excited vibrations in deep drilling systems, J. Sound Vib. 333 (mar 2014) 2019–2039.
[4] T. Richard, C. Germay, E. Detournay, Self-excited stick–slip oscillations of drill bits, Compt. Rendus Mec. 332 (aug 2004) 619–626.
[5] U.J.F. Aarsnes, N. van de Wouw, Dynamics of a distributed drill string system: characteristic parameters and stability maps, J. Sound Vib. 417 (mar 2018) 376–412.
[6] B. Besselink, T. Vromen, N. Kremers, N. van de Wouw, Analysis and control of stick-slip oscillations in drilling systems, IEEE Trans. Contr. Syst. Technol. 24 (1) (2016) 226–239.
[7] U.J.F. Aarsnes, O.M. Aamo, Linear stability analysis of self-excited vibrations in drilling using an infinite dimensional model, J. Sound Vib. 360 (jan 2016) 239–259.
[8] X. Liu, N. Vlajic, X. Long, G. Meng, B. Balachandran, State-dependent delay influenced drill string dynamics and stability analysis, in: 9th Int. Conf. Multibody Syst. Nonlinear Dyn. Control, vol. 7B, ASME, aug 2013, p. V07BT10A065.
[9] B. Besselink, N. van de Wouw, H. Nijmeijer, A semi-analytical study of stick-slip oscillations in drilling systems, J. Comput. Nonlinear Dynam. 6 (2) (2011) 021006.
[10] T. Richard, C. Germay, E. Detournay, A simplified model to explore the root cause of stick–slip vibrations in drilling systems with drag bits, J. Sound Vib. 305 (aug 2007) 432–456.
[11] C. Germay, N. van de Wouw, H. Nijmeijer, R. Sepulchre, Nonlinear drillstring dynamics analysis, SIAM J. Appl. Dyn. Syst. 8 (jan 2009) 527–553.
[12] K. Nandakumar, M. Wiercigroch, Stability analysis of a state dependent delayed, coupled two DOF model of drill-string vibration, J. Sound Vib. 332 (may 2013) 2575–2592.
[13] S.K. Gupta, P. Wahi, Global axial–torsional dynamics during rotary drilling, J. Sound Vib. 375 (aug 2016) 332–352.
[14] P. Wahi, A. Chatterjee, Self-interrupted regenerative metal cutting in turning, Int. J. Non Lin. Mech. 43 (mar 2008) 111–123.
[15] E. Detournay, P. Defourny, A phenomenological model for the drilling action of drag bits, Int. J. Rock Mech. Min. Sci. Geomech. Abstr. 29 (1) (1992) 13–23.
[16] R.J. LeVeque, Finite Volume Methods for Hyperbolic Problems, Cambridge university press, 2002.
[17] S. Patankar, Numerical Heat Transfer and Fluid Flow, CRC press, New York, NY, 1980.
[18] R. Courant, K. Friedrichs, H. Lewy, On the partial difference equation of mathematical physics, IBM J. Res. Dev. 11 (215–234) (1967) 32–74.
[19] T. Insperger, G. Stépán, J. Turi, State-dependent delay in regenerative turning processes, Nonlinear Dynam. 47 (nov 2006) 275–283.
[20] N. van de Wouw, E. Detournay, in: Proceedings of the Seconds Internation Colloquium on Nonlinear Dynamics and Control of Deep Drilling Systems (ICNDCDS 2012), 2012.
[21] S.K. Gupta, P. Wahi, Tuned dynamics stabilizes an idealized regenerative axial-torsional model of rotary drilling, J. Sound Vib. 412 (2018) 457–473.
[22] P.E. Pastusek, D. Ertas, L. Wang, J.R. Bailey, Drillstring mechanics model for surveillance, root cause analysis, and mitigation of torsional and axial vibrations, in: Proc. 2013 SPE/IADC Drill. Conf. Exhib., No. December, 2013.
[23] M. Ertas, E. Biediger, S. Sundararaman, J. Bailey, V. Gupta, N.-R. Bangaru, S. Bangaru, Methods and Systems for Mitigating Drilling Vibrations, 2009.
[24] R.J. Shor, M.W. Dykstra, O.J. Hoffmann, M. Coming, For better or worse: applications of the transfer matrix approach for analyzing axial and torsional vibration, in: SPE/IADC Drill. Conf. Exhib., 2015.
[25] J. Stecki, D. Davis, Fluid transmission lines distributed parameter models part 1: a review of the state of the art, Proc. Inst. Mech. Eng. Part A J. Power Energy 200 (4) (1986) 215–228.
[26] R.E. Goodson, R.G. Leonard, A survey of modeling techniques for fluid line transients, J. Basic Eng. 94 (2) (1972) 474.